Desalination and Water Treatment
www.deswater.com

doi: 10.5004/dwt.2020.24982

178 (2020) 220–239
February

Structural and surface modification of highly ordered alumina for enhanced removal of Pb^{2+}, Cd^{2+} and Ni^{2+} from aqueous solution

Dragana L. Milošević[a,*], Nataša Z. Tomić[b], Veljko R. Đokić[b], Milka M. Vidović[a], Zlate S. Veličković[c], Radmila Jančić-Heinemann[d], Aleksandar D. Marinković[d]

[a]*SI Institute of Chemistry, Technology and Metallurgy-National Institute, Center of Ecology and Technoeconomics, Njegoševa 12, 11001 Belgrade, Serbia, Tel. +38164 4555 472; email: milosevicdragana28@yahoo.com (D.L. Milošević), Tel. +38111 3370 474; email: mivibgd@yahoo.com (M.M. Vidović)*
[b]*Innovation Center, Faculty of Technology and Metallurgy, Karnegijeva 4, 11120 Belgrade, Serbia, Tel. +38111 3303 616; email: ntomic@tmf.bg.ac.rs (N.Z. Tomić), Tel. +381 11 3303 740; email vdjokic@tmf.bg.ac.rs (V.R. Đokić)*
[c]*Military Academy, University of Defense, Veljka Lukića Kurjaka 33, 11000 Belgrade, Serbia, Tel. +38165 2429 431; email: zlatevel@yahoo.com*
[d]*Faculty of Technology and Metallurgy, University of Belgrade, Karnegijeva 4, 11060 Belgrade, Serbia, Tel. +38111 3303 602; email: radica@tmf.bg.ac.rs (R. Jančić-Heinemann), Tel. +381 3303 750; email: marinko@tmf.bg.ac.rs (A.D. Marinković)*

Received 22 April 2019; Accepted 26 September 2019

ABSTRACT

The adsorption performance of three-dimensionally ordered macroporous (3DOM) alumina doped with iron oxide, and subsequently modified with (3-aminopropyl)triethoxysilane (APTES), $FeAl_2O_3$ and $FeAl_2O_3$APTES, was used for enhanced Pb^{2+}, Cd^{2+} and Ni^{2+} removal. The phase composition and the structural and surface/textural properties of the obtained adsorbents were analyzed by X-ray diffraction analysis, field emission scanning electron microscope, energy dispersive X-ray analysis, thermogravimetry, Fourier-transfer infrared spectroscopy, specific surface area of the samples and point of zero charge determination. Adsorption of selected cations was examined in the batch conditions using different contact time, adsorbent dosage and temperatures. Different models of the adsorption isotherms were used for determination of the adsorption capacities, in which the best fit of Freundlich and Langmuir model was obtained for $FeAl_2O_3$, that is, Freundlich model for $FeAl_2O_3$APTES. A significant increase of adsorption capacities: from 44.21 to 51.66 mg g^{-1} for Pb^{2+}, 25.69 to 32.96 mg g^{-1} for Cd^{2+} and 19.48 to 24.64 mg g^{-1} for Ni^{2+} was obtained for $FeAl_2O_3$ and $FeAl_2O_3$APTES, respectively, which indicated the significance of the macroporous structure of 3DOM alumina and subsequent amino-terminal modification. The values of the correlation coefficient (R^2) suggested that pseudo-second kinetic model best describes Pb^{2+}, Cd^{2+} and Ni^{2+} adsorption on $FeAl_2O_3$APTES, and Cd^{2+} and Ni^{2+} onto $FeAl_2O_3$, while second kinetic model gave the highest correlation coefficients for Pb^{2+} adsorption on $FeAl_2O_3$.

Keywords: Alumina; Sol-gel processes; Surface properties; Adsorption

* Corresponding author.

1. Introduction

Problems of heavy metal pollution in the natural resources were followed by the growth of population and industrial development [1–3]. Increasing discharge of heavy metals, such as lead, cadmium, nickel, chromium, mercury, etc. in industrial wastewaters, which are released into recipients, is a growing concern. Therefore, to protect the environment and human health, dangerous environmental pollutants which include heavy metals should be removed from industrial effluents before they are discharged into the environment. Until now numerous techniques, for heavy metal removal, such as membrane processes [4–6] or chemical processes [7] have been developed. Most of these methods have had disadvantages regarding costs and among all adsorption technology was found to be one of the most commonly used due to the simplicity and cost-effectiveness [8–10].

Thanks to the large specific surface area, pore size distribution, mechanical and acid–base properties, alumina was widely studied as a material for many applications such as sorption [11–15], catalysis, [16,17] and supercapacitor electrodes [18]. It is well known that the performance of alumina largely depends on its textural properties and crystalline structure. Beside different crystal structures of alumina [19], such as δ, θ, η, α, γ, etc., the most attention was caught by α and γ-alumina. The fabrication of three-dimensionally ordered architectures of materials (3DOM) with macroporous arrays with nano-/microstructured surfaces is of great importance for a wide range of use. Some of the strategies to synthesize 3DOM alumina in different forms (powders, films, etc.) are focused on nano casting processes [20,21], anodization [22,23], dip-coating method [24,25], modified sol-gel route [26], etc. In order to increase the adsorption capacity of alumina, it is necessary to find new methods for structural and surface modification of alumina [12,27–29]. Generally, the main constituent of alumina is a large number of hydroxyl groups that are capable to interact with adsorbate via electrostatic interactions, ion exchange, complexation, etc. [30]. Possible cation binding mechanisms at the surface of alumina are dependent on surface charges and hydroxyl group number [30]. Beside adsorptive sites present in the alumina surface, modification with amino groups are very important for the improvement of adsorption capacities [31,32].

This paper is focused on the research of 3DOM alumina as an adsorbent for the efficient removal of selected heavy metals. The structural modification of adsorbents is carried out by doping alumina with iron oxide ($FeAl_2O_3$) following with further surface modification using amino silane coupling agent (APTES). The results of adsorption tests have been investigated by taking into consideration the time of adsorption, pH value of the solution, adsorbent mass and temperature. Two specific goals, achieved by introduction of a significant number of amino groups in $FeAl_2O_3$APTES, was: (1) effective cation removal due to their high affinity with respect to cation and (2) creation of reactive/versatile functionalities suitable for further modification or covalent attachment on different support to obtain new adsorbent with improved adsorption performance and higher potential for application in a real water purification system. Different adsorption kinetic models including pseudo-first order, pseudo-second order, second order, intraparticular Dunwald–Wagner (D–W), intraparticular homogenous diffusion solid (HDSM), Roginsky-Zeldovich-Elovich (Elovich) and Weber–Morris (W–M) adsorption kinetics have been examined to model the adsorption processes.

2. Experimental part

2.1. Materials and chemicals

MilliQ deionized water (DW) with 0.05 μS cm^{-1} conductivity was used in all experiments. Standard solutions of Pb^{2+}, Cd^{2+} and Ni^{2+} (1,000 mg L^{-1}, Accu Trace™ Reference Standard, USA) were further diluted with DW to the concentration of ~10 mg L^{-1}. Crystallized aluminum(III)-pentahydroxy chloride ($Al_2(OH)_5Cl{\cdot}2.5H_2O$) was purchased from the Clariant AG Chemicals Company, Switzerland. Anhydrous iron(III)-chloride ($FeCl_3$), (powder, ≥99.99% trace metals basis), (3-Aminopropyl)triethoxysilane 99% (APTES) and methanol were used, which were purchased from Sigma-Aldrich Chemie, GmbH. Lipoxol 6000 (poly(ethylene glycol)-PEG, Sasol Performance Chemicals, GmbH) was used as a dispersing agent. Toluene (dried over sodium wire), HNO_3 and NaOH were supplied from Fisher Scientific, UK.

2.2. Synthesis, structural and surface modification of alumina adsorbents

Poly(methylmethacrylate) (PMMA) microspheres, used as a pore-forming agent, and 3DOM alumina doped with iron-oxide ($FeAl_2O_3$) were synthesized analogously to the procedure described in previous work [33]. A precursor of $FeAl_2O_3$ was obtained by preparation of solution Al^{3+}/Fe^{3+} salts: $Al_2(OH)_5Cl{\cdot}2.5H_2O/FeCl_3$ = 100/10 w/w with the addition of PMMA microspheres porogen and thermally processed at the controlled condition to obtain structurally modified three-dimensionally ordered macroporous $FeAl_2O_3$ adsorbent.

Synthesis of $FeAl_2O_3$ was performed according to the following procedure: solution of a dispersing agent (PEG) was obtained by dissolving 3 g of PEG in 6 mL solution of water/EtOH mixture (1.5:4.5 v/v) at room temperature under stirring. A solution of the aluminum(III)pentahydroxy chloride was obtained by dissolving 14.56 g of $Al_2(OH)_5Cl{\cdot}2.5H_2O$ in 12 mL of DW followed by the addition of 1.45 g anhydrous $FeCl_3$ to obtain a mixture of Al^{3+}/Fe^{3+} ions. PMMA microspheres (4.25 g) were dispersed in 2.0 mL of dispersing agent and 3.35 mL solution of Al^{3+}/Fe^{3+} ions mixture under stirring at 700 rpm for 5 min. The suspension was filtrated under vacuum through a Teflon filter paper in order to remove residual water. The filtrate was dried at 45°C for 48 h. The dried filtrate, named $FeAl_2O_3$, was calcined with a heating rate of 1°C min^{-1} from room temperature to 800°C and held for 5 h at this temperature, followed by cooling at a rate of 1°C min^{-1}.

Structurally modified alumina, $FeAl_2O_3$, was used as a media for linkage of silane coupling agent APTES. Condensation of $FeAl_2O_3$ and APTES was performed by mixing 500 mg $FeAl_2O_3$ and 530 μL of APTES in 10 mL of dry toluene at 70°C for 20 h. The precipitate was separated by centrifugation and dried at 45°C for 24 h. The obtained adsorbent was named $FeAl_2O_3$APTES.

2.3. Characterization methods

Fourier-transfer infrared spectroscopy (FTIR) analysis of samples was performed using Thermo Scientific Nicolet 6700 spectrometer in the attenuated total reflectance (ATR) mode. The range of wavenumber was 4,000–500 cm^{-1}.

The phase composition of the samples was determined by X-ray diffraction technique (XRD), (Model Philips PW1710 diffractometer, Co Kα radiation).

The energy dispersive X-ray analysis (EDAX) of the samples $FeAl_2O_3$ and $FeAl_2O_3$APTES was performed by using Jeol JSM 5800 Sem (Oxford Link Isis 300).

The microstructure and morphology of the obtained samples were studied, after providing conductivity by sputtering samples with a thin golden layer, using a Tescan Mira3 XMU field emission scanning electron microscope (FE-SEM) operated at 20 kV.

The specific surface area of the samples (S_{BET}), pore volume and pore size distribution of samples are determined based on nitrogen adsorption–desorption isotherm measured at 77.4 K using a Micromeritics ASAP 2020 V1.05H surface area analyzer, (Micromeritics Instrument Corp., USA).

The thermal stability of the samples was investigated by non-isothermal thermogravimetric analysis (TGA) using a SETARAM SETSYS Evolution 1750 instrument. The measurements were conducted at a heating rate of 10°C min^{-1} in a dynamic argon atmosphere (flow rate 20 $cm^3\ min^{-1}$) in the temperature range of 30°C–800°C.

The concentrations of heavy metal ions (Pb^{2+}, Cd^{2+} and Ni^{2+}) were measured by atomic absorption spectrometry using a PinAAcle 900T, PerkinElmer Inc. USA instrument according to the standard testing method 3111B [34].

A laboratory pH meter, InoLab Cond 730 precision conductivity meter (WTW GmbH), with an accuracy of ±0.01 pH units, was used for the pH measurements. The pH values at the point of zero charges (pH_{pzc}) were measured using the pH drift method, before and after metal adsorption according to the literature [35,36].

Amino group content (AN) was determined via "back² (indirect) titration. 10 mg of alumina-based adsorbents were placed in 10 mL 0.01 mol L^{-1} HCl and ultrasonicated for 15 min. Materials were then filtered, and 10 mL of supernatant was titrated with a standard solution of 0.01 mol L^{-1} KOH in the presence of Methyl Orange. Aforementioned technique is based on the reaction of the reactant with unknown concentration (amino group) and reactant in surplus with a known concentration (HCl, 0.01 mol L^{-1}). The amount of excess HCl is determined with NaOH titration. The amount of amino group that reacted with HCl is determined based on the difference of the total amount of HCl used to treat $FeAl_2O_3$ and $FeAl_2O_3$APTES (10 mL) and the amount of HCl determined with KOH titration [36].

2.4. Adsorption and kinetic experiments

Batch adsorption experiments were performed by equilibration of Pb^{2+}, Cd^{2+}, and Ni^{2+} adsorbate solution under magnetic stirring in order to evaluate the performance of the modified highly ordered alumina-based adsorbents. Adsorption equilibrium experiments were performed by addition of 1, 2, 3, 4, 5, 6, 7 and 10 mg of adsorbent in a vials of 10 mL containing 10.8, 10.0 and 10.68 mg L^{-1} of standard solutions of Pb^{2+}, Cd^{2+} and Ni^{2+} ions, respectively. Initial pH value, that is, pH_i, was changed in the range 2–10, and optimal one was defined at pH_i 6. Thermodynamic parameters were calculated from adsorption equilibrium experiments performed at 25°C, 35°C and 45°C. The adsorption kinetics was studied by varying the contact time in the range from 0 to 24 h at the same initial concentrations, $m/V \approx$ 150–1,500 mg L^{-1}, pH_i 6 at 25, 35 and 45°C. The suspensions after adsorption were filtered through a nylon membrane syringe filter with pore size 0.22 μm. The quantity of Pb^{2+}, Cd^{2+} and Ni^{2+} adsorbed per mass unit of the adsorbent was calculated from Eq. (1) [33]:

$$q = \frac{\left(C_i - C_f\right)}{m} V' \tag{1}$$

where q is the adsorption capacity in mg g^{-1} adsorbent, C_i and C_f are the initial and final concentrations of ions in the solution in mg L^{-1}, V' is the volume of solution in L, and m is the mass of the adsorbent in g. Based on the calculated values of q, adsorption isotherms are determined as the dependence of q, mg g^{-1} from equilibrium concentration C_e, mg L^{-1}. Obtained results were compared with four models of adsorption isotherms (Langmuir, Freundlich, Temkin and Dubinin–Radushkevich (D–R) models).

3. Results and discussion

The research work is focused on characterization of obtained adsorbents $FeAl_2O_3$ and $FeAl_2O_3$APTES, and further on equilibrium, kinetic and thermodynamic aspect of adsorption removal of Pb^{2+}, Cd^{2+} and Ni^{2+} with consideration of the adsorption mechanism.

The phase composition and the structural and surface/textural properties of the obtained modified samples were analyzed by FTIR, S_{BET}, pH_{PZC}, XRD, FE-SEM, EDAX and TG analysis.

3.1. Structure characterization via FTIR spectroscopy

The structure of synthesized adsorbents, $FeAl_2O_3$ and $FeAl_2O_3$APTES, before and after adsorption, was examined by ATR-FTIR spectroscopy, Fig. 1.

Al-O stretching vibrations were noticed in the range of 500–1,000 cm^{-1}, which indicated the γ-crystalline structure [37]. Characteristic peaks at ≈616 and ≈733 cm^{-1} pointed to stretching vibrations of Al–O bonds in which aluminum could be either tetrahedrally or octahedrally coordinated [38]. Structural change of γ-alumina by iron concomitantly introduces hydroxyl groups bound to coordinated Al atoms. Thermal treatment reduces the number of surface hydroxyl groups and thus influence the adsorption capacity of adsorbents. The lower intensities OH stretching bands in $FeAl_2O_3$ at 3,550 and 3,470 cm^{-1} became more intense and sharper after adsorption of cations onto $FeAl_2O_3$, (Fig. 1a), which could be related to the different interaction hydroxyl/cation (proton-accepting oxygen non-bonding lone electron/cation) to change the force constant of the OH stretching vibration [33]. The peak at 1,638 cm^{-1} originates from OH bending

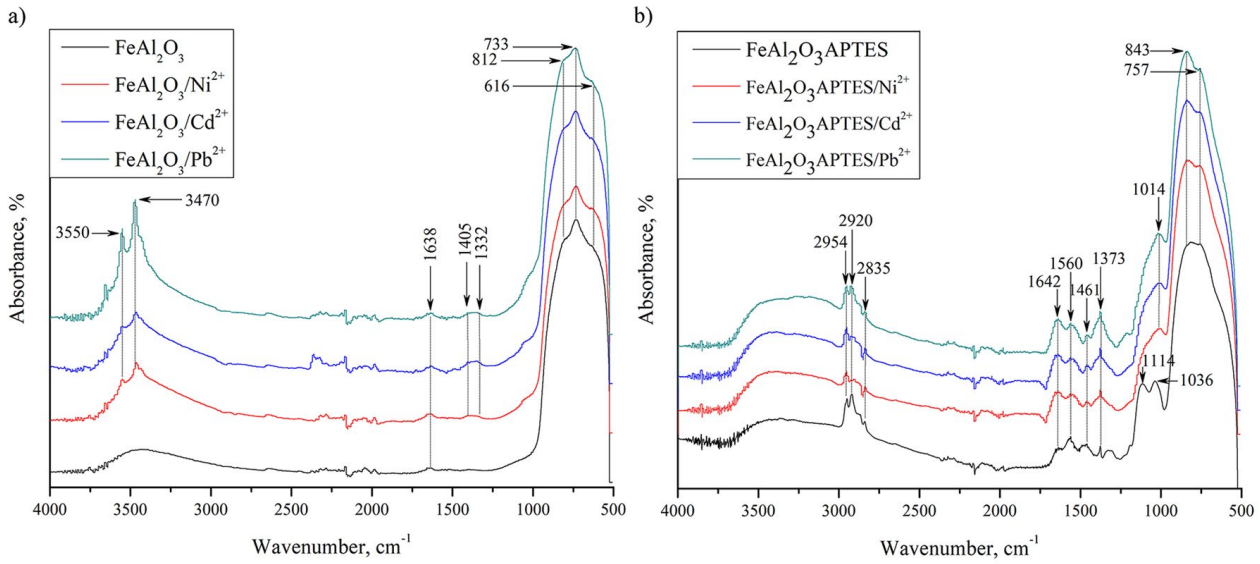

Fig. 1. FTIR spectra of (a) $FeAl_2O_3$ and (b) $FeAl_2O_3$APTES before and after adsorption experiment.

vibration, while the peak at ≈3,470 cm^{-1} is attributed to the stretching vibration of OH surface functional group [39,40] and has not significantly changed after adsorption of Pb^{2+}, Cd^{2+} and Ni^{2+}. In the ATR-FTIR spectra of $FeAl_2O_3$APTES in Fig. 1b besides the absorption bands of vibration frequencies of OH and Al–O groups, the appearance of new bands associated with successful APTES modification was observed. The peaks at 2,954, 2,920 and 2,835 cm^{-1} are associated with stretching vibrations of C–H groups. The C–H in-plane bending vibrations of CH_3, symmetrical and asymmetrical, are observed at 1,373 and 1,461 cm^{-1}, respectively. The band observed at 1,014 and 1,036 cm^{-1} is due to Si–O stretching vibration. Siloxane group (Si–O–Si) is shown as stretching mode at 1,114 cm^{-1} obtained by condensation of APTES on alumina surface.

In addition, the bands at 1,461 and 1,114 cm^{-1}, corresponding to N–H in-plane and C–N bond stretching vibration, respectively, overlapped with C–H vibration. The broad peaks at 3,300–3,600 cm^{-1} were due to the NH_2 stretch of the amine group overlapped with OH stretching vibration. A band at ≈800 cm^{-1} was not observable, attributed to the out-of-plane NH_2 bending vibration [41], which could be most indicative of the type of adsorption mechanism.

3.2. pH_{pzc} and textural properties of the highly-ordered $FeAl_2O_3$ and $FeAl_2O_3$APTES

The pH of the point of zero charges, that is, pH_{pzc}, and textural properties of the samples are given in Table 1.

Results from Table 1 show that specific surface area of $FeAl_2O_3$ was lower than 3DOM alumina obtained without doping with iron oxide (77.3 $m^2 g^{-1}$) [33]. Also, somewhat decreased values of textural parameters of $FeAl_2O_3$APTES (Table 1), that is, decrease of specific surface area and mean diameter of the mesopore was a result of deposition of APTES on the exterior/interior surface of $FeAl_2O_3$. Overall system porosity was determined according to Eqs. (2)–(4), and

Table 1
pH_{pzc} and textural properties of $FeAl_2O_3$ and $FeAl_2O_3$APTES

Parameter	Sample	
	$FeAl_2O_3$	$FeAl_2O_3$APTES
pH_{pzc}	7.10	6.70
Specific surface area, S_{BET} ($m^2 g^{-1}$)	64.60	60.56
Total pore volume, V_{total} ($cm^3 g^{-1}$)	0.18	0.16
Mesopore volume, V_{meso} ($cm^3 g^{-1}$)	0.17	0.15
Mean mesopore diameter, D_{mean} (nm)	204.60	192.80

estimated to be 78% and 74% for $FeAl_2O_3$ and $FeAl_2O_3$APTES, respectively. Obtained results indicate high porosity of both adsorbents with large average pore diameter (Table 1), which are important prerequisite to obtain high-performance adsorbent.

The particle porosity, ε_p, can be calculated as described in [42] using Eq. (2).

$$\varepsilon_p = \frac{V - \frac{m}{\rho_m}}{V} \tag{2}$$

where V is volume of the wet sample, mL, m is mass of the dry sample, g, ρ_m is material density, g mL^{-1}. The volume of the wet sample, V, and material density, ρ_m, were obtained using Eqs. (3) and (4).

$$V = V_1 - \frac{m_1 - m_2}{\rho_{H_2O}} \tag{3}$$

where V_1 is volume of the pycnometer, 15 mL, m_1 is mass of the pycnometer after being filled with water, g, m_2 is mass of the pycnometer with wet sample, g, ρ_{H_2O} is water density, 1 g mL^{-1}.

$$\rho_m = \frac{m}{V - \frac{m_3 - m}{\rho_{H_2O}}} \quad (4)$$

m_3 is mass of wet sample, g.

A significant number of total basic sites of 0.20 mmol g^{-1}, with a predominance of an amino group, potentially means a higher probability for cations interaction/binding with surface functionalities.

Introduction of amino groups causes a small decrease of pH_{pzc} for $FeAl_2O_3$APTES, comparing with $FeAl_2O_3$, which is the result of surface modification by APTES. For adsorption of cations onto a $FeAl_2O_3$ and $FeAl_2O_3$APTES, the active sites should be deprotonated, which is achieved when the pH value of the solution is higher than pH_{pzc}. At $pH > pH_{pzc}$ negatively charged adsorbent surface beneficially attracts positively charged species. Also at pH > 6 for Pb^{2+} and at pH > 8 for Ni^{2+} and Cd^{2+} insoluble metal hydroxide precipitate causing interference in obtaining realistic adsorption results. In contrast to this, when $pH < pH_{pzc}$ active sites are protonated, the surface of the material is positively charged, and adsorption of metal ions is suppressed by competition with H^+ ion and electrostatic repulsion with the positively charged surface. In accordance with the presented results and the fact that pH of most natural water is in the range from 5 to 7 operational pH was established at 6 throughout all adsorption experiments.

3.3. XRD analysis

X-ray diffraction was employed for the determination of the crystallinity of the highly ordered $FeAl_2O_3$ calcined at 800°C and after modification ($FeAl_2O_3$APTES), Fig. 2. Formation of the α phase was followed by dehydration and desorption of surface hydroxyl groups at the temperature of calcination at 800°C [43]. According to the diffractogram in Fig. 2, the amorphous wall of a mesostructure is converted to γ-alumina phase (JCPDS Card No. 10–0425) [44]. In contrast to previous work, which describes partially crystalline alumina showing a lower degree of long-range structural order [33], the obtained XRD pattern reflects the improved crystalline structure of face-centered cubic γ-alumina being produced after treatment at 800°C by addition of Fe^{3+} ions. The presence of larger and more emphasized peaks on the XRD pattern imply better crystallization of the $FeAl_2O_3$ compared with neat Al_2O_3. Diffractogram in Fig. 2 shows that the modification with APTES causes no structural change of $FeAl_2O_3$APTES sample.

3.4. SEM analysis of the microstructure of $FeAl_2O_3$ and $FeAl_2O_3$APTES adsorbents

The fact that PMMA microspheres formed ''opal'' structure and his infiltration in synthesized material, followed by removal with the calcination, was used to yield the ''inverse opal'' structure of $FeAl_2O_3$ which is shown in SEM micrograph in Fig. 3a. SEM analysis of three-dimensional structure

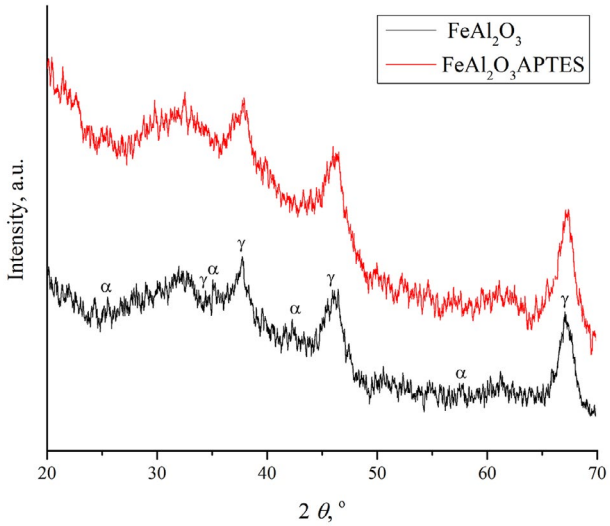

Fig. 2. XRD pattern of $FeAl_2O_3$ and $FeAl_2O_3$APTES sample.

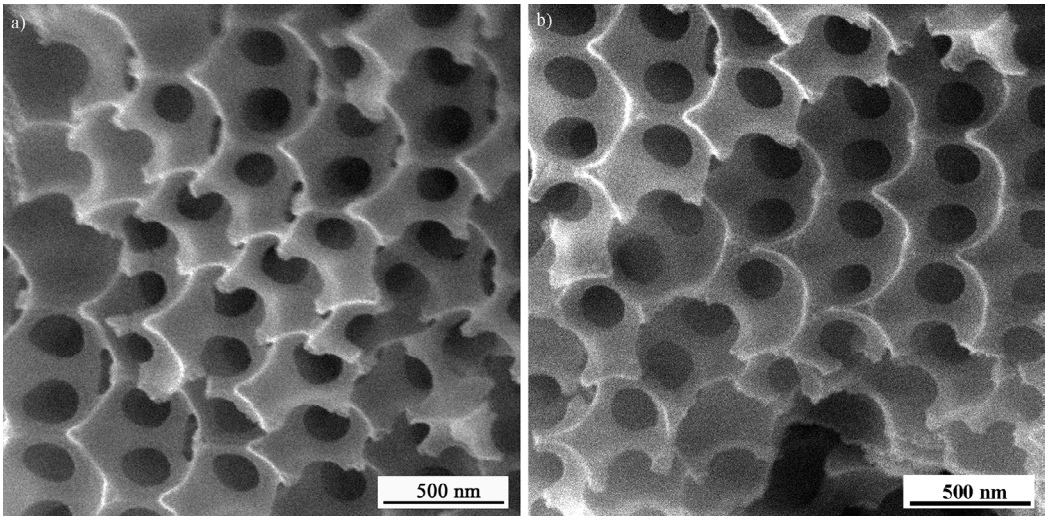

Fig. 3. FE-SEM images of (a) $FeAl_2O_3$ and (b) $FeAl_2O_3$APTES.

of $FeAl_2O$ and $FeAl_2O_3$APTES showed low shrinkage [33] after calcination and textural properties change after modification with APTES. By comparing Figs. 3a and b, it was found that in the presence of APTES molecules, samples retained the same morphology with insignificant pore reduction (Table 1). It can be seen that the amination treatment does not cause a significant change in surface structure and pore size reduction. FE-SEM analysis showed a highly ordered structure of 3DOM $FeAl_2O_3$ with a hardly observable surface coverage of $FeAl_2O_3$APTES formed by a silane coupling agent.

3.5. Energy dispersive X-ray analysis

EDAX spectra of both adsorbents (Figs. 4a and b) confirmed the presence of C, O, Al and Fe in the $FeAl_2O_3$, and C, O, Al, Fe, N and Si, in $FeAl_2O_3$APTES. Along with EDAX spectra, values of the contents of these elements in the tested area are also given (Table 2). Taking into account the results of the XRD analysis, it can be said that Fe in both samples is dominantly in the amorphous form, whether it is elemental Fe or the ionic of Fe(II) or Fe(III) form.

Results of EDAX showed that surface content of Si indicates effective and controlled modification of $FeAl_2O_3$ by silane. In accordance to result of overall alumina modification, that is, amino number value of 0.20 mmol g^{-1}, indicate, on a theoretical basis, that ~44 mg g^{-1} (4.4 %) of silane was introduced. This result is similar to the one found in the literature [18] and higher than suggested by well-known producer [45] to obtain monolayer coverage of APTES. Such achievement is very important to provide the optimal extent of alumina surface modification, that is, self-assembled monolayer with multilayer participation of multilayered silane coverage, with the highest adsorption capacity. In that way, high adsorption performance at the lowest consumption of expensive silane modifying agent was obtained.

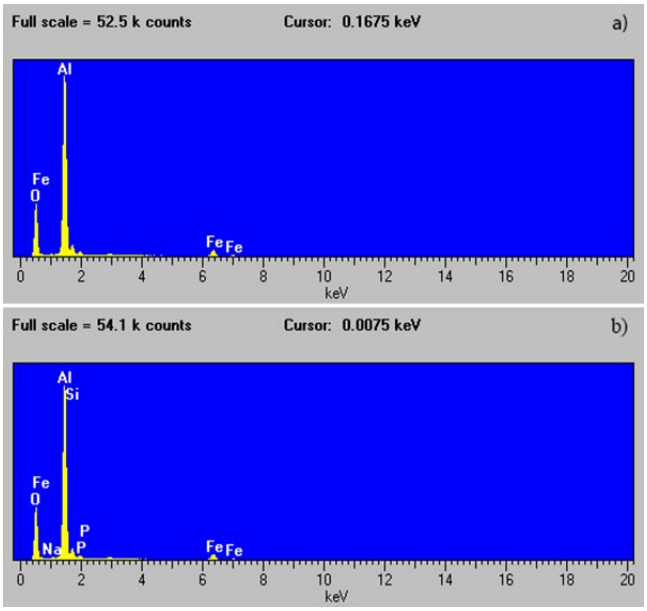

Fig. 4. EDS spectrum of (a) $FeAl_2O_3$ and (b) $FeAl_2O_3$APTES.

3.6. Thermal analysis

The TG/DTG thermograms of the obtained $FeAl_2O_3$ precursor, alumina after calcination at 800°C and modified alumina with APTES, are shown in Fig. 5.

The $FeAl_2O_3$ precursor exhibited three decomposition steps during the calcination. Small decrease in weight (4.3 wt%, Fig. 5a) with decomposition peak at 52°C (Fig. 5b) was observed due to the removal of adsorbed water and ethanol used for dissolving $Al_2Cl(OH)_5$ and PEG which were not removed by drying. A decrease in weight (20.3 wt.%) at 288°C with decomposition peak at 382°C is related to the decomposition of $Al_2Cl(OH)_5$ and the removal of PEG and the PMMA template [33]. The residue after 800°C (19.8 wt.%) indicated that the entire PMMA template was removed and crystal structure was formed, after calcination at 800°C, leaves alumina residue.

TGA of $FeAl_2O_3$ sample indicated only release of physically adsorbed water at alumina surface with a peak at 92°C (Fig. 5c). The weight loss of $FeAl_2O_3$APTES sample occurred in two stages. The first stage of mass loss occurred at a temperature range between 30°C and 110°C (Fig. 5c), which could be related to the loss of physically adsorbed water that was not removed by drying. The second region showed the weight loss between 110°C and 500°C, with a decomposition peak at 409°C (Fig. 5c) indicating the decomposition temperature of the free (non-hydrolyzed) ethoxy groups with the liberation of unsaturated alkyl fragments. The TGA data confirmed the presence of 2 wt.% of the thermally degradable structure, that was related to bonded APTES. This result was defined from the difference between $FeAl_2O_3$APTES and $FeAl_2O_3$ TGA residue of 92.0 and 94.0 wt.%, respectively (Fig. 5). Also, a calculation based on APTES surface residue and an amino number gave an approximative density of ~1.8 APTES residue per nm^2. Attachment procedure provided a condition for monolayer-like coverage with appropriate extent of the formation of multilayered structure based on APTES [46].

3.7. Equilibrium study of Pb^{2+}, Cd^{2+} and Ni^{2+} adsorption on $FeAl_2O_3$ and $FeAl_2O_3$APTES

Among many adsorption parameters important for the definition of operational condition, pH_i, that is, initial pH,

Table 2
Element content derived from EDS spectrum of the $FeAl_2O_3$ and $FeAl_2O_3$APTES

Element	$FeAl_2O_3$	$FeAl_2O_3$APTES
	mas. %	
C	3.60	6.36
O	50.96	47.78
Al	37.72	34.58
Fe	7.71	6.47
Si	–	3.81
Na	–	0.36
P	–	0.63
N	–	0.30
Total	100.00	100.00

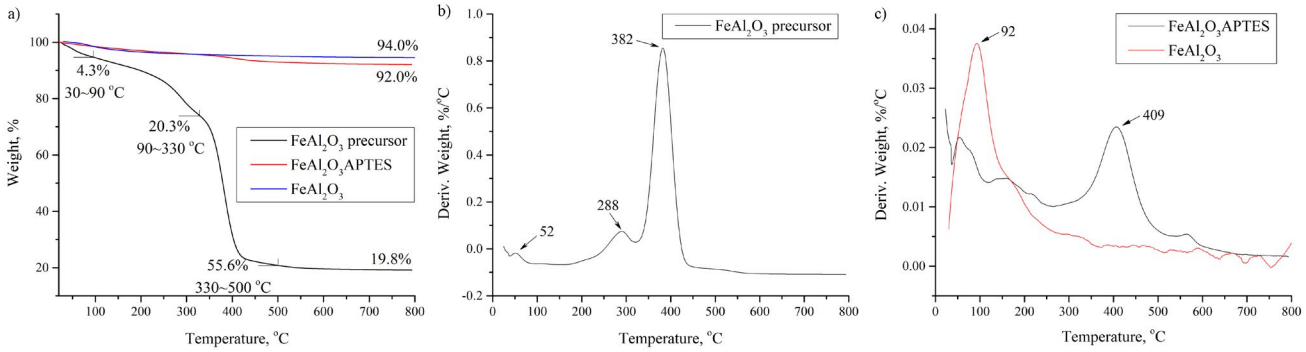

Fig. 5. (a) Thermogravimetric (TG), (b) differential thermal gravimetric (DTG) analysis of $FeAl_2O_3$ precursor and (c) differential thermal gravimetric (DTG) analysis of $FeAl_2O_3$ and $FeAl_2O_3$APTES.

is one of the parameters which determine the solubility/speciation of ions, degree/extent of the ionization of adsorbent, that is, protonation/deprotonation of the adsorbent functional groups, the concentration of counter ions during the adsorption. The differences in the effectiveness of ion removal as a function of pH could be generally explained by the metal speciation diagrams shown in Fig. 6. The most favorable adsorption region was defined at pH < 6 for Pb^{2+} and pH < 8 for Cd^{2+} and Ni^{2+}. Preliminary determination of the adsorption efficiency vs. pH_i showed a similar trend as in previous study [33] and thus pH_i of 6 was used in all subsequent experiments. The benefit of such selection is in good agreement with the pH of most natural water, which is in the range 5–7, and could be subjected to purification processes without pH adjustment of influent water.

As example lead speciation in water solution could be present by equilibria of different forms of Pb^{2+}, $Pb(OH)^+$, $Pb(OH)_2$ and $Pb(OH)_3^-$ at different pH values. Equilibrium concentrations of Pb^{2+} ionic species, at different pH, could be calculated from appropriate constants (log *K*) for hydrolysis reactions at 25°C and the precipitation constant of $Pb(OH)_2$(s) (1.2×10^{-15}) (given in Fig. 6). Precipitated $Pb(OH)_2$ at pH higher than 8 was calculated theoretically and experimentally, and subtracted from the overall available amount of Pb^{2+} ions, and thus reliable adsorption results were obtained. Similar discussion stands for the ionic speciation of Ni^{2+} and Cd^{2+} ions.

Another important parameter in the adsorption process is adsorbent dosage. In order to examine the effect of adsorbent dosage, the amount of adsorbent was changed from 1 to 10 mg. The removal efficiency of Pb^{2+}, Cd^{2+} and Ni^{2+} at the temperature of 25°C using $FeAl_2O_3$ adsorbent (1.50 g L^{-1}), were 95.7%, 96.3% and 86.0%, respectively (Fig. 7). Similar results for $FeAl_2O_3$APTES adsorbent at the same temperature and mass ratio was 98.1%, 96.2% and 84.5% (Fig. 7). Analogously, Bhat et al. [47] noticed that at the higher adsorbent dosage, the adsorption efficiency of γ-alumina nanoparticles to remove Pb^{2+} ions was significantly enhanced. The increase of adsorption surface sites followed by an increase of adsorbent dosage resulted in higher adsorption efficiency [48].

The state of adsorption equilibria was analyzed from the results of different adsorption isotherm fitting in order to calculate the adsorption capacity of the prepared materials, $FeAl_2O_3$, and $FeAl_2O_3$APTES, for Pb^{2+}, Cd^{2+} and Ni^{2+} ion removal. Comparison of the obtained results was examined with four models of adsorption isotherms, that is, the Langmuir, Eq. (5) [49], Freundlich Eq. (6) [48], Dubinin–Radushkevich (D–R), Eq. (8) [50] and Temkin, Eq. (9) isotherms. Results of the non-linear fitting, obtained for $FeAl_2O_3$ and $FeAl_2O_3$APTES, are shown in Table 3.

Langmuir and Freundlich's isotherms are the most commonly used model for the fitting of adsorption data. Langmuir isotherm means the formation of a monolayer on the homogeneous adsorption surface and the adsorption of each molecule has equal adsorption activation energy. Freundlich isotherm signifies heterogeneous surface with uneven adsorption heat distribution with the possibility of the existence of multi-layered adsorption [35].

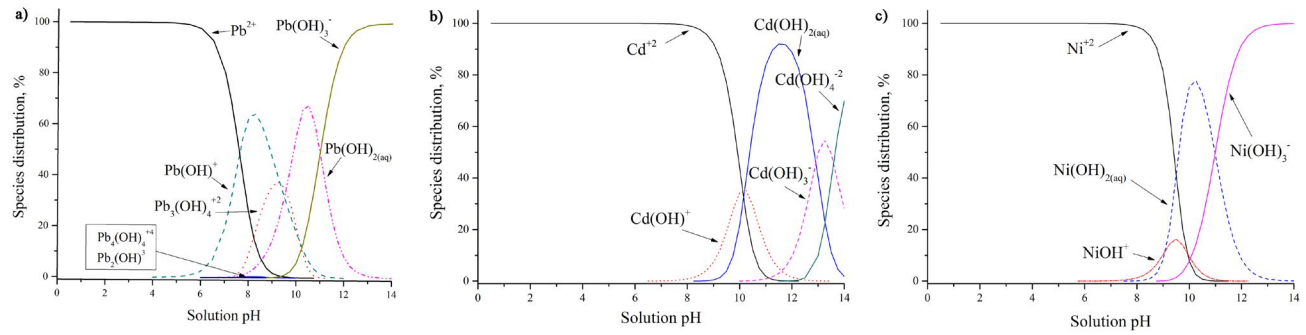

Fig. 6. Speciation of (a) Pb^{2+}, (b) Cd^{2+} and (c) Ni^{2+} obtained using MINTEQ 3.0 software (C = 25 mg L^{-1}, t = 25°C) [33].

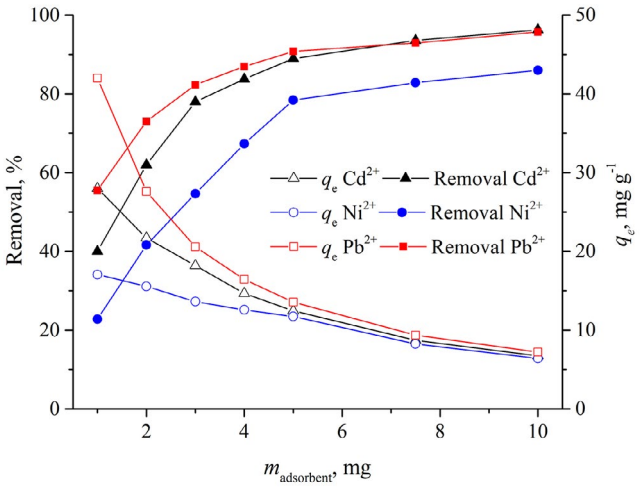

Fig. 7. Removal (%) and q_e of Pb^{2+}, Cd^{2+} and Ni^{2+} on the $FeAl_2O_3$ at pH_i = 6 and different adsorbent dose, m_{ads} = 1, 2, 3, 4, 5, 7 and 10 mg.

$$q_e = \frac{q_m K_L C_e}{1 + K_L C_e} \text{ or linear form } \frac{C_e}{q_e} = \frac{1}{K_L q_m} + \frac{C_e}{q_m} \quad (5)$$

$$q_e = K_F C_e^{\frac{1}{n}} \text{ or linear form } \log q_e = \log K_F + \frac{1}{n}\log C_e \quad (6)$$

where C_e is equilibrium metal ion concentration left in the solution (mg L^{-1}); q_e is adsorbed amount of metal ions (mg g^{-1}); q_m and K_L are Langmuir constants related on the adsorption capacity and adsorption energy. Maximum adsorption capacity, q_m, denotes the amount of adsorbate, so the complete adsorption surface is covered with adsorbate monolayer (mg g^{-1}), and K_L (L mol^{-1}) is the constant related with the adsorption heat.

In Freundlich model (Eq. (6)), K_F is an approximate indicator of the adsorption capacity for the equilibrium concentration, and $1/n$ is the Freundlich adsorption intensity parameter, that is, it defines the strength of adsorption. For n = 1 the partition between the two phases are independent of the concentration, $1/n < 1$ indicates normal adsorption, while for $1/n > 1$ indicates cooperative adsorption.

Among the adsorption parameters calculated using Eq. 5, the adsorption capacity, q_m, and affinity, K_L, are the most important ones used for the analysis of adsorption process and selection of operational conditions. The K_L parameter from Eq. (5) can be used to calculate a dimensionless separation factor (R_L) by the following equation [51,52].

$$R_L = \frac{1}{1 + K_L \times C_i} \quad (7)$$

where C_i represents initial Pb^{2+}, Cd^{2+} and Ni^{2+} concentrations. Based on the R_L values, the adsorption could be irreversible

Table 3
Adsorption isotherm parameters for $FeAl_2O_3$ and $FeAl_2O_3$APTES (C_i~10 mg/L, t = 24 h, m/V = 150–1,500 mg/L, pH = 6.0 for Pb^{2+}, Cd^{2+} and Ni^{2+})

Model/parameter		Pb^{2+}			Cd^{2+}			Ni^{2+}		
		25°C	35°C	45°C	25°C	35°C	45°C	25°C	35°C	45°C
					$FeAl_2O_3$					
Langmuir isotherm	q_m, mg g^{-1}	44.21	47.44	49.91	25.69	27.76	29.27	19.48	20.90	23.15
	K_L, L mol^{-1}	344,152.9	375,411.1	460,843.8	412,957.6	444,335.1	493,904.7	137,389.1	151,998.4	185,102.4
	K_L, L mg^{-1}	1.660	1.811	2.224	3.674	3.953	4.394	2.341	2.589	3.154
	R_L	0.056	0.052	0.043	0.026	0.025	0.022	0.041	0.037	0.031
	R^2	0.927	0.929	0.933	0.902	0.901	0.908	0.973	0.903	0.970
Freundlih isotherm	K_F, (mg g^{-1}) (L mg^{-1})$^{1/n}$	23.731	26.162	29.221	17.982	18.954	19.822	12.999	13.223	14.197
	n^{-1}	0.369	0.370	0.362	0.249	0.263	0.269	0.228	0.260	0.267
	R^2	0.998	0.997	0.995	0.977	0.982	0.980	0.917	0.939	0.932
					$FeAl_2O_3$APTES					
Langmuir isotherm	q_m, mg g^{-1}	51.66	53.92	56.71	32.96	35.43	39.50	24.64	26.46	29.65
	K_L, L mol^{-1}	617,246.73	731,994.09	907,792.93	301,906.4	330,980.91	350,111.39	67,086.0	78,136.8	81,560.9
	K_L, L mg^{-1}	2.978	3.532	4.381	2.686	2.944	3.114	1.143	1.331	1.319
	R_L	0.032	0.028	0.022	0.036	0.033	0.031	0.080	0.070	0.067
	R^2	0.913	0.909	0.896	0.880	0.921	0.946	0.878	0.894	0.908
Freundlih isotherm	K_F, (mg g^{-1}) (L mg^{-1})$^{1/n}$	32.942	36.135	40.534	20.575	22.455	25.186	12.099	13.581	15.018
	n^{-1}	0.354	0.349	0.344	0.313	0.309	0.317	0.348	0.342	0.353
	R^2	0.997	0.998	0.998	0.998	0.990	0.981	0.996	0.994	0.994

(R_L = 0), favorable (0 < R_L < 1), linear (R_L = 0) or unfavorable (R_L > 1).

The Dubinin–Radushkevich (D–R) isotherm model was used to predict the nature of adsorption processes as physical or chemical by calculating sorption energy. The linear form of this model is described by Eq. (8) [50]:

$$\ln q_e = \ln q_m - B(RT)^2\left[\ln\left(1+\frac{1}{C_e}\right)\right]^2 \quad (8)$$

where B (mol^2 kJ^{-2}) is D–R constant which is determined as the slope of ln q_e vs. [RT ln(1 + 1/C_e)]^2, and the intercept yields the adsorption capacity q_m (mg g^{-1}).

The Temkin isotherm model is described by Eq. (9) [53]:

$$q_e = \frac{RT}{b}\ln(AC_e) \text{ or linear form } q_e = \frac{RT}{b}\ln A + \frac{RT}{b}\ln C_e \quad (9)$$

where A is Temkin isotherm equilibrium binding constant (L g^{-1}) and b is Temkin isotherm constant.

Graphical presentations of Langmuir and Freundlich isotherm model fitting are given in Figs. 8 and 9 for both adsorbents.

The high adsorption capacities of both $FeAl_2O_3$ and $FeAl_2O_3$APTES adsorbents were due to available continual porosity and surface functionalities of both ordered alumina adsorbents. Complex porous network, that is, interconnected macropores and mesopores with a high contribution of gigapores [54], contribute to the easy availability of surface functionalities with low diffusional resistance to adsorbate transport. Additionally, improved adsorption performances of $FeAl_2O_3$APTES are the results of a number of introduced amino functionalities. Results from Table 3 indicate that the Freundlich isotherm model fitted well Pb^{2+}, Cd^{2+} and Ni^{2+} adsorption on $FeAl_2O_3$APTES, thus it is clear that the adsorption took place forming a heterogeneous structure with multilayer coverage. This result is in accordance with amino number determination and TGA analysis. The reciprocal value of the Freundlich isotherm constant, 1/n, amounted to 0.1 < 1/n < 1 indicated favorable adsorption of Pb^{2+}, Cd^{2+} and Ni^{2+} on $FeAl_2O_3$APTES. Freundlich isotherm model fitted well Pb^{2+} and Cd^{2+}, while the Langmuir isotherm model gave the best fitting for Ni^{2+} adsorption on $FeAl_2O_3$ (Table 3). Standard error (SE) data analysis for the adsorption of Pb^{2+}, Cd^{2+} and Ni^{2+} on $FeAl_2O_3$ and $FeAl_2O_3$APTES, using Langmuir and Freundlich isotherms, is given in Table 4.

Also, results from Temkin and D–R model fitting are given in Table 5. Comparing with the structurally modified sample, $FeAl_2O_3$, surface modified sample, $FeAl_2O_3$APTES, lead to an increase of adsorption capacities for all three metal ions. Also comparing with our previous work [33] where

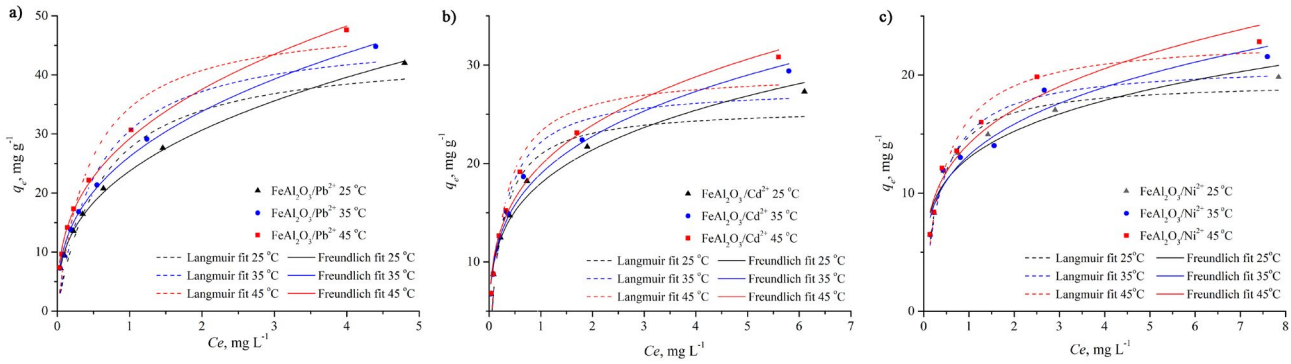

Fig. 8. Freundlich and Langmuir adsorption isotherms for (a) Pb^{2+}, (b) Cd^{2+} and (c) Ni^{2+} on the $FeAl_2O_3$ at pH$_i$ = 6 at 25°C, 35°C and 45°C.

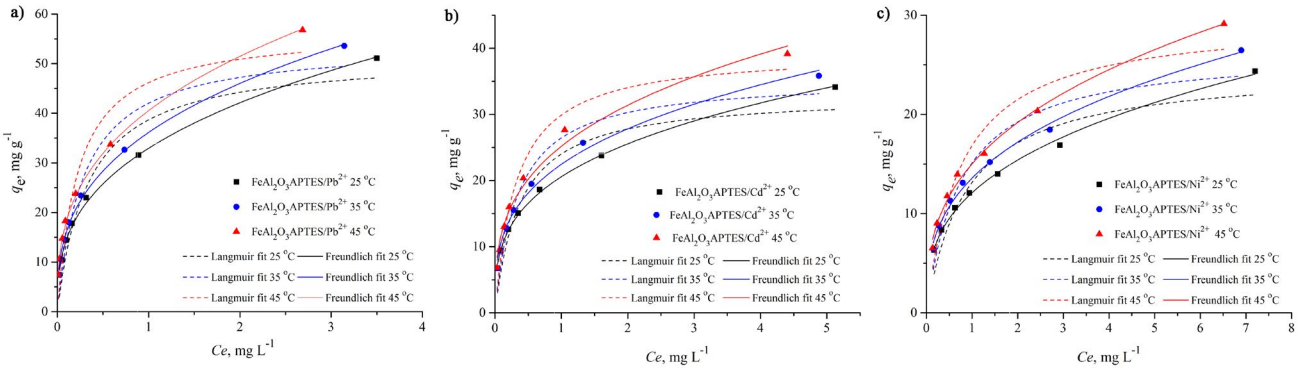

Fig. 9. Freundlich and Langmuir adsorption isotherms for (a) Pb^{2+}, (b) Cd^{2+} and (c) Ni^{2+} on the $FeAl_2O_3$APTES at pH$_i$ = 6 at 25°C, 35°C and 45°C.

pure Al_2O_3 was used for adsorption of the same ions, and at the same temperatures, significant improvement in the adsorption capacities for Cd^{2+} and Ni^{2+} was achieved, while adsorption capacities for Pb^{2+} were lower for both materials.

3.8. Thermodynamics of the adsorption

In order to study temperature influence on the adsorption processes three different temperatures, 25°C, 35°C and 45°C, were selected. The Gibbs free energy ($\Delta G°$), enthalpy ($\Delta H°$) and entropy ($\Delta S°$) for Pb^{2+}, Cd^{2+} and Ni^{2+} ions adsorption were calculated according to Van't Hoff equations (Eqs. (10) and (11)) [55].

$$\Delta G° = -RT\ln\left(K_L\right) \tag{10}$$

$$\ln\left(K_L\right) = \frac{\Delta S°}{R} - \frac{\Delta H°}{\left(RT\right)} \tag{11}$$

where T is the absolute temperature in K, and R is universal gas constant (J mol^{-1} K^{-1}). Langmuir adsorption constant K_L

Table 4
Standard error (SE) data analysis for the adsorption of Pb^{2+}, Cd^{2+} and Ni^{2+} on $FeAl_2O_3$ and $FeAl_2O_3$APTES

Model	Value	Pb^{2+}			Cd^{2+}			Ni^{2+}		
		25°C	35°C	45°C	25°C	35°C	45°C	25°C	35°C	45°C
					$FeAl_2O_3$					
Langmuir	SE (q_m)	4.262	4.591	4.625	1.936	2.236	2.329	0.631	1.444	0.949
	SE (K_L)	0.449	0.491	0.587	1.257	1.150	1.081	0.392	0.657	0.329
Freundlich	SE (K_F)	0.248	0.284	0.419	0.457	0.446	0.503	0.540	0.533	0.619
	SE (n)	0.057	0.059	0.081	0.273	0.228	0.503	0.559	0.419	0.434
					$FeAl_2O_3$APTES					
Langmuir	SE (q_m)	5.307	5.724	6.469	3.396	2.998	2.857	2.582	2.544	2.792
	SE (K_L)	0.907	1.128	1.537	0.895	0.786	0.682	0.351	0.383	0.361
Freundlich	SE (K_F)	0.380	0.369	0.364	0.176	0.433	0.694	0.166	0.216	0.251
	SE (n)	0.067	0.060	0.052	0.063	0.142	0.190	0.080	0.097	0.097

Table 5
Adsorption isotherm parameters for $FeAl_2O_3$ and $FeAl_2O_3$APTES (C_i~10 mg/L, t = 24 h, m/V = 750 mg/L, m_{ads} = 1, 2, 3, 4, 5, 7 and 10 mg, pH = 6.0 for Pb^{2+}, Cd^{2+} and Ni^{2+})

Model/parameter		Pb^{2+}			Cd^{2+}			Ni^{2+}		
		25°C	35°C	45°C	25°C	35°C	45°C	25°C	35°C	45°C
					$FeAl_2O_3$					
Temkin isotherm	A, L g^{-1}	35.850	40.180	48.969	99.098	94.917	91.654	116.49	84.696	64.247
	b, mg g^{-1}	7.40	7.83	8.21	4.23	4.47	4.73	2.60	2.91	3.28
	B	334.93	327.28	322.08	586.34	572.60	559.72	954.16	879.23	807.54
	R^2	0.951	0.947	0.951	0.988	0.985	0.982	0.952	0.965	0.975
D-R	q_m, mg g^{-1}	27.27	28.71	31.04	20.74	21.47	22.24	15.39	16.20	17.20
	B, mol^2kJ^{-2}	8.94	8.88	8.81	8.60	8.56	8.53	8.25	8.19	8.13
	E_a, kJ mol^{-1}	7.480	7.502	7.535	7.625	7.641	7.657	7.786	7.811	7.839
	R^2	0.836	0.835	0.856	0.872	0.866	0.861	0.964	0.958	0.958
					$FeAl_2O_3$APTES					
Temkin isotherm	A, L g^{-1}	68,081	89.718	124.47	59.512	60.787	59.335	17.509	19.511	19.120
	b, mg g^{-1}	8.41	8.52	8,71	5.47	5.95	6.73	4.60	4.98	5.60
	B	294.64	300.66	303.80	452.81	430.90	393.19	539.14	514.13	472.55
	R^2	0.949	0.944	0.940	0.962	0.977	0.981	0.954	0.966	0.969
D-R	q_m, mg g^{-1}	33.66	35.28	37.91	23,15	25.10	27.91	16.56	18.45	20.35
	B, mol^2 kJ^{-2}	8.73	8.68	8.61	8.49	8.41	8.30	8.17	8.07	7.97
	E_a, kJ mol^{-1}	7.570	7.590	7.622	7.675	7.711	7.761	7.821	7.873	7.922
	R^2	0.836	0.835	0.856	0.872	0.866	0.861	0.964	0.958	0.958

is calculated from isothermal experiments (Table 3). $\Delta H°$ and $\Delta S°$ are calculated from slopes and interceptions in diagram $\ln(K_L)$–T^{-1}, assuming that the system attained stationary conditions. The quality of data fitting is confirmed with high R values and low values of standard errors (Table 4).

Negative values of Gibbs free energy changes ($\Delta G°$) indicate the spontaneity of Pb^{2+}, Cd^{2+} and Ni^{2+} adsorption on $FeAl_2O_3$ and $FeAl_2O_3$APTES, Table 6 [56]. Results obtained from Table 6 for $\Delta G°$ are in agreement with results from Table 3 where higher spontaneity of Pb^{2+}, Cd^{2+} and Ni^{2+} ions adsorption on both materials was obtained.

The $\Delta H°$ does vary significantly between studied ions with the highest values found for Pb^{2+}. Positive enthalpy (ΔH) not greater than 15.19 kJ mol^{-1} for all examined metal ions and both samples, pointed to physical adsorption. The low value of $\Delta H°$ indicates low influence of temperature on adsorption effectiveness, that is, low to moderate increase of q_e was found (Table 6).

Low endothermic nature of the process could be the result of the difference between energy consumed by desolvation of $[M(H_2O)_6]^{2+}$ ion, and liberated energy from the formation of an M^{2+}/amino complex [3,31,56]. The summary contribution of different elementary adsorption processes, either diffusional or adsorption/desorption at the adsorbent surface, with prevailing endothermic character of desolvation process, resulted in low positive values of $\Delta H°$.

The positive values of $\Delta S°$ (Table 6) indicate an appropriate increase of randomness at the adsorbent/solution interface due to numerous energetically different intermolecular interactions which are mostly electrostatic in nature. The highest value of $\Delta S°$ found for Pb^{2+} could be explained by the higher value of ionic radii and thus different packing/interaction in a multilayered structure at the adsorbent surface. The dominant mechanism in the sorption process was dissociative because the value of the entropy changes for all metal ions was positive [57].

3.9. Adsorption mechanism of Pb^{2+}, Cd^{2+} and Ni^{2+} ions removal by the $FeAl_2O_3$ and $FeAl_2O_3$APTES

Based on the results of equilibrium and kinetic data mechanism of adsorption onto $FeAl_2O_3$ and $FeAl_2O_3$APTES was considered as a complex process with the contribution of the electrostatic interactions, ion exchange and lowest contribution could be M^{2+} ions occupying free vacancies in the structure of the alumina. Structural modification of alumina causes appropriate extent of crystal lattice distortion, and due to this higher efficiency of $FeAl_2O_3$ modification with APTES is a consequence. According to obtained results and literature data [3,31,41,56], it was assumed that the possible mechanism of adsorbate bonding involves electrostatic interactions/complexation, as is given in Fig. 10.

The hydroxyl and amino groups located on the surface of $FeAl_2O_3$ and $FeAl_2O_3$APTES, respectively, are sites able to participate in a Pb^{2+}, Cd^{2+} and Ni^{2+} ions removal (Fig. 10). In general, the adsorption mechanism and structure of bonded cations at the $FeAl_2O_3$ and $FeAl_2O_3$APTES surface are affected by protonation/deprotonation equilibria of surface groups and adsorbate speciation at operational pH. Analysis of bonding types was also discussed in relation to results obtained in this work and literature finding [30,31,56,58].

Adsorption processes and cation binding mechanisms at $FeAl_2O_3$ surface is dependent on surface charges and hydroxyl group number. The pH_{pzc} of both $FeAl_2O_3$ and $FeAl_2O_3$APTES (Table 1) is higher than the pH_i of heavy metal solutions, which indicates that the surface of both materials are mainly negatively charged, suggesting that some repulsion of the cation with positive surface charges could take place. Before adsorption, initial pH values of the Pb^{2+}, Cd^{2+} and Ni^{2+} solutions were adjusted to pH_i 6.0, and after system equilibration slight decrease of final pH was observed (in the range 0.1–0.3 unit), and depend on the amount of used adsorbent and ion of interest due to mainly electrostatic attraction [30].

The mechanism of ions adsorption on $FeAl_2O_3$ and $FeAl_2O_3$APTES could be explained by the exchange of hydrogen from surface hydroxyl groups. Results of NMR, infrared spectroscopic electrical conductivity [59] and potentiometric studies of oxide surface immersed in water provide evidence that the oxide surface, populated with hydroxide functional group, behave as weak acids and bases. Due to amphoteric character surface hydroxyl could react with electron-deficient cation by forming either surface complexes or ion pair assembly due to electrostatic interactions, depicted as shown by Eqs. (12) and (13):

$$\mathrm{AlOH} + \mathrm{M}^2 \rightarrow \left(\mathrm{AlO}^-\right)\mathrm{M}^+ + \mathrm{H}^+ \tag{12}$$

$$2\mathrm{AlOH} + \mathrm{M}^{2+} \rightarrow \left(\mathrm{AlO}^-\right)_2 \mathrm{M}^+ + 2\mathrm{H}^+ \tag{13}$$

Table 6
Calculated Gibbs free energy, enthalpy and entropy for $FeAl_2O_3$ and $FeAl_2O_3$APTES

			$\Delta G°$, kJ mol^{-1}		$\Delta H°$, kJ mol^{-1}	$\Delta S°$, J mol^{-1}	R^2
Adsorbent	Ion	25°C	35°C	45°C			
$FeAl_2O_3$	Pb^{2+}	–41.56	–43.17	–45.12	11.46	177.65	0.939
	Cd^{2+}	–42.01	–43.61	–45.30	7.04	164.47	0.984
	Ni^{2+}	–39.28	–40.86	–42.71	11.71	170.88	0.959
$FeAl_2O_3$APTES	Pb^{2+}	–43.01	–44.89	–46.91	15.19	195.1	0.993
	Cd^{2+}	–41.23	–42.85	–44.39	5.85	157.97	0.986
	Ni^{2+}	–37.50	–39.15	–40.54	7.75	151.92	0.916

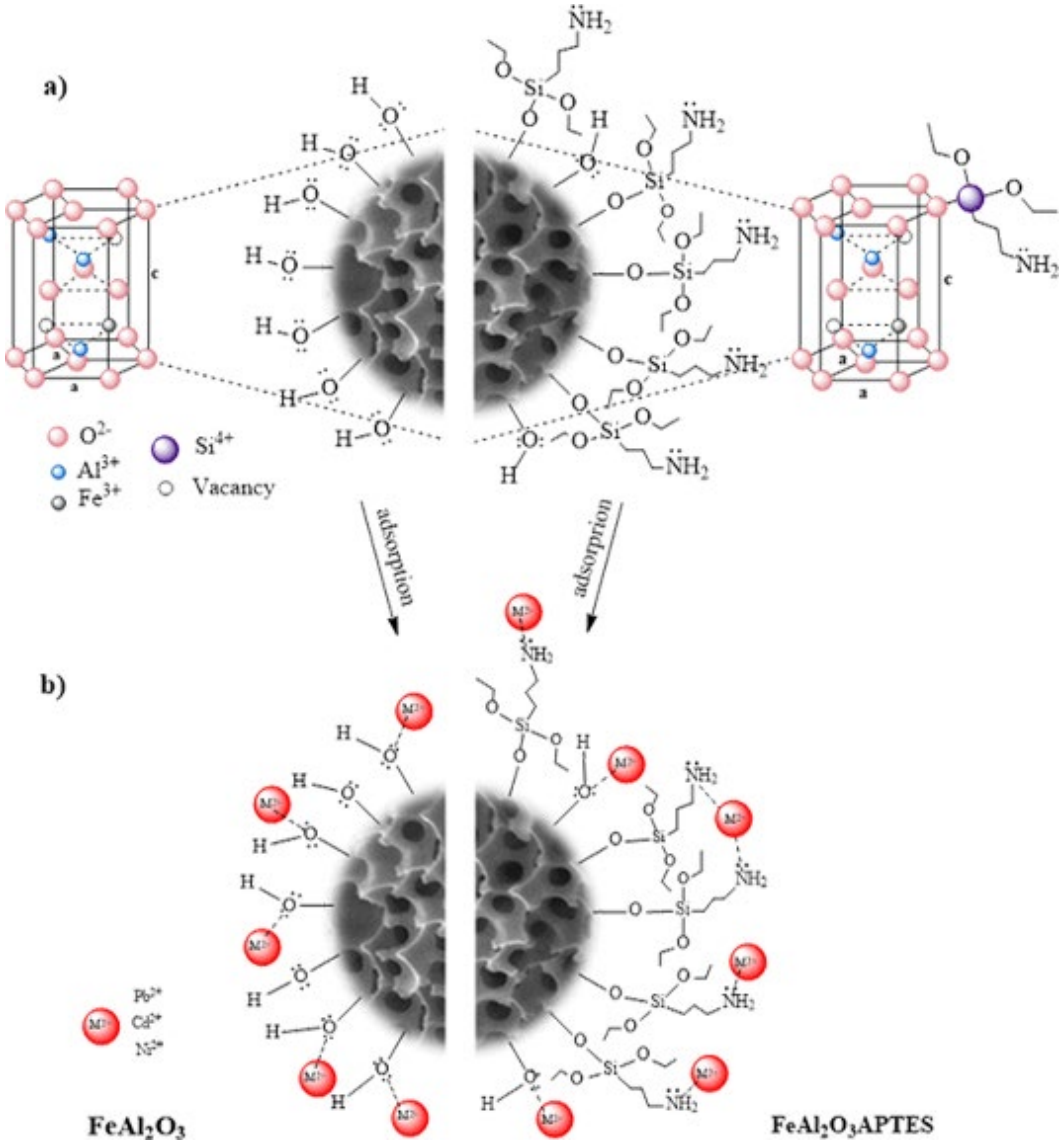

Fig. 10. Schematic presentation of (a) structure and surface functionalities of $FeAl_2O_3$ and $FeAl_2O_3$APTES, and (b) bonding mechanism of cations M^{2+} (Pb^{2+}, Cd^{2+} and Ni^{2+}) on both adsorbent.

Cations adsorption, according to Eqs. (12) and (13), cause the simultaneous release of H^+ and creation of a coordinative complex with hydroxyl groups. Two options could be operative: cation with hydration sphere could occupy a position in the outer plane of charge distribution profile which is termed as "outer sphere" complexes. On the other hand, ions that lose a part or all their hydration spheres and bonded directly to the oxide, the surface is termed as "inner sphere" complexes. The cation is more tightly bounded to hydroxyl group present in the inner coordination sphere of the double layer as a result of geometric adaption of complex caused by surface structure and protonation/deprotonation processes. Obtained results are consistent with the formation of inner-sphere complexes with and it was also proved that Pb^{2+} bonds to one oxygen of the oxide surface [60].

The shift of pH_{pzc} of γ-alumina adsorbent after adsorption was explained by higher activity of the counter ions at the outer surface that compensates accumulation of the surface charge generated by specific cation adsorption, that is, formation of inner-sphere complexes [33]. Analogous results were obtained in the present study.

Except for the participation of adsorptive sites present on $FeAl_2O_3$ surface also amino groups in $FeAl_2O_3$APTES additionally play an important role in processes of cation removal. Binding capability and mechanism of cation to amino groups were clearly evidenced and discussed [31]. In general, the electron-donating capability of amino group as *N*-donor determines the extent of delocalization of the p electron of the metal atom over ligand structure. Results of theoretically calculated potential curves for cyclic Cd-ethylene diamine (Cd/cis-EDA) and non-cyclic (Cd/trans-EDA) complexes, considering binding and total energies, were found to be larger for cyclic, both the triplet and singlet state over the distances considered. The formation of more stable Cd(cis-EDA)

complex was enabled by structural arrangement from the non-cyclic to cyclic structure [61].

Structural determination of Cd^{2+} EDA complexes, performed according to ^{113}Cd NMR spectra recording, showed that, except $[Cd(H_2O)_6]^{2+}$, and hydrated mono, bis and tris Cd/EDA complexes, that is, $[Cd(EDA)]^{2+}$, $[Cd(EDA)_2]^{2+}$ and $[Cd(EDA)_3]^{2+}$, respectively, was formed [62].

Also detailed study on binding capabilities of multi-walled carbon nanotube modified with ethylenediamine, diethylenetriamine and triethylenetetramine modified multi-walled carbon nanotubes (raw-MWCNT, o-MWCNT, e-MWCNT, d-MWCNT and t-MWCNT, respectively) was used for Pb^{2+} and Cd^{2+} ions removal. It was shown that coordination and electrostatic interactions between cations and unprotonated amino groups are the main adsorption mechanism. Preferential binding capabilities of the cation with the primary amino groups, compared with a secondary amino group, relate to higher nucleophilicity of the former, and a binding mechanism was established by complexation and chelation [36,63]. Obtained results also indicate the significance of introduced primary amino groups.

Lead removal experiments on siliceous SBA-15 mesoporous adsorbent, that is, SBA-15 substrate functionalized with APTES at optimal condition, was performed in the range of pH 5–6 with achieving a high removal efficiency of 93%. The bonding mechanism after Pb(II) adsorption was studied using UV–Vis and XPS spectroscopies and found van der Waals electrostatic cation/NH_2 groups through the ion exchange. Amino group concentration was deduced from N/Si atomic ratios (XPS spectra) and found that at low lead concentration inner pore network was mainly occupied, while at higher concentration, that is, 400 ppm, external surface is mainly occupied [58]. In line with literature results, it is clear that amino group present electron-donating site which shows high affinity with respect to the divalent metal cation.

3.10. Kinetic studies

There are numerous mathematical models used for the description of the kinetic process of adsorption, that is, used the analysis of adsorption mechanism. According to recent literature data, the most suitable models for describing the sorption of ions on solid adsorbents are pseudo-first, pseudo second and second order model.

The pseudo-first order, that is, Lagergren rate equation, is based on solid capacity. Its linear form is given by Eq. (14) [64]:

$$\ln\left(q_e - q_t\right) = \ln q_e - k_1 t \tag{14}$$

where k_1 (min^{-1}) is the pseudo-first rate constant, q_t (mg g^{-1}) is the adsorption capacity at time t (min), and q_e (mg g^{-1}) is the value of adsorption capacity at equilibrium. The linear form of pseudo-second order equation [65,66] is expressed by Eq. (15):

$$\frac{t}{q_t} = \frac{1}{k_2 q_e^2} + \frac{1}{q_e} \tag{15}$$

where k_2 (g mg^{-1} min^{-1}) is the second-order rate constant, q_t (mg g^{-1}) and q_e (mg g^{-1}) are the adsorption capacities at any time t and at equilibrium, respectively. The initial sorption rate h_2 (mg g^{-1} min^{-1}) at $t \to 0$ is calculated as:

$$h_2 = k_2 q_e^2 \tag{16}$$

The results of non-linear correlation coefficients, using pseudo-first, pseudo-second and second kinetic rate law, are given in Table 7.

The values of the correlation coefficient (R^2) suggested that second kinetic model best describes Pb^{2+}adsorption on $FeAl_2O_3$, while pseudo-second order (Eq. (15)) gave the highest correlation coefficients for Cd^{2+} and Ni^{2+} onto $FeAl_2O_3$ and Pb^{2+}, Cd^{2+} and Ni^{2+} onto $FeAl_2O_3$APTES. Value of R^2 on the $FeAl_2O_3$APTES for Ni^{2+} had almost the same values for all three model used. In the case of the pseudo-second order (PSO) equation, three consecutive steps are operative in the course of adsorption: (1) the diffusion of cation from bulk solution to the exterior adsorbent surface; (2) the diffusional transport of cation into the pore network; and (3) the adsorption/desorption equilibria at the interior adsorbent surface. It was also suggested that all three steps could be of appropriate contribution with the most significant first two steps [67]. Presented results suggested that the second and third step could be the most significant while both pollutant and adsorbent surface functionalities concentration determine overall adsorption kinetics.

In order to determine kinetic activation parameters, determination of PSO rate constant was performed at 25°C, 35°C and 45°C, and obtained kinetic data were used for calculation of activation parameters using a linearized form of Arrhenius equation, given by Eq. (17):

$$\ln k_2' = -\frac{E_a}{RT} + \ln A' \tag{17}$$

where k_2' is reaction rate constant, E_a denotes activation energy, R is universal gas constant (8.314 J mol^{-1} K^{-1}), T is the temperature in Kelvin, A' is Arrhenius factor (frequency factor). Calculated kinetic activation parameters are presented in Table 8.

Calculated activation energy could indicate on operative adsorption mechanism. In the physical adsorption, the equilibrium is usually rapidly attained and easily reversible because the energy requirement is small (E_a = 0–40 kJ mol^{-1}) and since the forces involved are weak [49]. The values of activation energy for Pb^{2+}, Ni^{2+} and Cd^{2+} indicate that the adsorption of all three metal ions onto alumina-based adsorbents is a physical adsorption process. The process of Pb^{2+} adsorption onto $FeAl_2O_3$APTES could be better described by a pseudo-second order kinetic model which implies the existence of different adsorption mechanisms, such as ion exchange, complexation and electrostatic interactions.

3.11. Analysis of diffusional processes

Modeling of kinetic data according to the PSO kinetic law does not provide a deeper understanding of the rate-limiting adsorption step. The definition of kinetic law which could

Table 7
Kinetic parameters for $FeAl_2O_3$ and $FeAl_2O_3$APTES adsorbents (C_i = 10.8, 10.0 and 10.68 mg L^{-1} for Pb^{2+}, Cd^{2+} and Ni^{2+}, respectively; t = 120 min, m/V = 715 mg/L, pH = 6)

	Ion	Parameter	Pseudo-first	Pseudo-second	Second-order
$FeAl_2O_3$	Pb^{2+}	q_e	14.650	17.119	17.120
		k (k_1, k_2)	0.023608	0.001226	0.004212
		R^2	0.952	0.967	0.992
	Cd^{2+}	q_e	12.137	16.278	16.278
		k (k_1, k_2)	0.016099	0.000948	0.003590
		R^2	0.987	0.990	0.969
	Ni^{2+}	q_e	10.062	13.409	13.409
		k (k_1, k_2)	0.005727	0.002165	0.001423
		R^2	0.912	0.994	0.958
$FeAl_2O_3$APTES	Pb^{2+}	q_e	28.228	20.730	20.730
		k (k_1, k_2)	0.052662	0.001200	0.020050
		R^2	0.846	0.999	0.911
	Cd^{2+}	q_e	13.53603	17.492	17.492
		k (k_1, k_2)	0.017188	0.000716	0.004282
		R^2	0.980	0.983	0.966
	Ni^{2+}	q_e	11,905	15.867	15.867
		k (k_1, k_2)	0.030642	0.001510	0.002799
		R^2	0.968	0.967	0.959

Table 8
Activation energy of $FeAl_2O_3$ and $FeAl_2O_3$APTES for Pb^{2+}, Cd^{2+} and Ni^{2+} adsorption

Metal	$FeAl_2O_3$	$FeAl_2O_3$APTES
	E_a, kJ mol^{-1}	
Pb^{2+}	7.575	6.467
Cd^{2+}	8.412	8.260
Ni^{2+}	14.632	9.676

be useful for analysis of mass transport phenomena was the next task considered in order to estimate the extent of diffusional limitation either in a batch or fixed packed-bed column study. Thus the evaluation of a rate-limiting step was performed according to the results obtained from the diffusional kinetic equation [68]. Multi-step nature of adsorption processes could be controlled by bulk diffusion, boundary layer diffusion, intra-particle diffusion and surface adsorption. The first step linear part demonstrates external mass transfer from the bulk solution to the most available adsorptive sites at the outer adsorbent surface. The second and the third parts of the adsorption process significantly depend on adsorbent porosity, that is, pore structure and geometry and network density. Due to the concentration gradient, the ions diffuse through the bulk solution and tree-like system of macro-, meso- and micropores, extending into adsorbent interior to reach all available surface active sites. The intra-particle resistance slows down adsorbate transport, that is, net transport in the direction of a variable time-dependent concentration gradient. At the final stage of the process, the adsorption takes place at a low rate until the saturation of all available surface sites is achieved.

In order to elucidate the possible chemisorption process for systems with the heterogeneous adsorbing surface, the following simplified form of Elovich equation [69] was used:

$$q_t = \frac{1}{b'}\ln(ab) + \frac{1}{b'}\ln t \tag{18}$$

where q_t (mg g^{-1}) represents the adsorption capacity at any time t, a is initial Pb^{2+}, Cd^{2+} and Ni^{2+} adsorption rate (mg g^{-1} min^{-1}), while b' is related to the extent of surface coverage and activation energy for chemisorption (g mg^{-1}). An approaching equilibrium factor R_E obtained from dimensionless Elovich equation [70] is defined as:

$$R_E = \frac{1}{q_{\text{ref}} b'} \tag{19}$$

where q_{ref} is the solid-phase concentration at time t_{ref} which is the longest time in adsorption process. According to the classification of characteristic curves based on R_E derived from the Elovich equation [70], there are four types of characteristic curves, depending on R_E value: if $R_E > 0.3$, then the curve rises slowly; if R_E is between 0.1 and 0.3, the curve rises mildly (mild adsorption); the value of R_E between 0.02 and 0.1 indicate rapid adsorption and when $R_E < 0.02$, the curve instantly approaches equilibrium.

In the case where internal diffusion is the rate-limiting step, then the kinetic data can be well correlated using following Weber and Morris equation [71]:

$$q_t = k_i t^{\frac{1}{2}} + C_{\text{BL}} \tag{20}$$

where k_i (mg g^{-1} min$^{1/2}$) is intraparticle diffusion rate constant and C_{BL} is constant related to the thickness of the boundary layer. If the intraparticle diffusion is the sole rate-limiting step, then the plot of q_t vs. $t^{1/2}$ would result in a linear relationship and would pass through the origin. The values of intraparticle diffusion rate k_i and C_{BL} can be obtained from the slope of q_t vs. $t^{1/2}$ plot.

Dunwald–Wagner (D–W) [72] was initially used for the study of reactions between a solid and a gaseous phase, considering the slowest step in the process is diffusion into or out of the solid particles, with special care on consideration of contribution of intra-particular transport inside particles [73]. D–W relation could be presented by Eqs. (21) and (22):

$$\frac{q_t}{q_e} = 1 - \frac{6}{\pi^2}\sum_{n=1}^{\infty}\frac{1}{n^2}\exp\left[-n^2 Kt\right] \tag{21}$$

where K (min^{-1}) is the rate constant of adsorption. Simplification of Eq. (21) gives:

$$\log\left(1-\left(\frac{q_t}{q_e}\right)^2\right) = -\frac{K}{2.303}t \tag{22}$$

A plot of $\log(1-(q/q_t)^2)$ vs. t should give linear plot and the rate constant can be calculated from the slope of correlation line. D-W was reasonably used to describe different kinds of adsorption systems and estimation of adsorption kinetics. Serin and Ellickson [74] expressed the D–W equation in terms of the partial completion of the reaction Eq. (23):

$$k_{DW}t = \frac{\pi^2}{r'^2}Dt = \ln\frac{6}{\pi^2\left(1-\alpha\right)} = -\log\left(1-\left(\frac{q_t}{q_e}\right)^2\right) \tag{23}$$

where r' is the initial radius of the reacting particle, α is the fractional completion of reactions at time t, D is the diffusion coefficient of the migrating species and k_{DW} is the Dunwald–Wagner isothermal reaction constant, q_e and q_t are the adsorption capacity of adsorbent (mg g^{-1}) at equilibrium and appropriate t, respectively.

A typical intra-particle diffusion model is the homogeneous diffusion solid model (HDSM), which can describe mass transfer in an amorphous and homogeneous sphere [75], and can be presented by following differential equation:

$$\frac{\partial q}{\partial t} = \frac{D_s}{r^2}\frac{\partial}{\partial r} = \left(r^2\frac{\partial q}{\partial r}\right) \tag{24}$$

where D_s is intraparticle diffusion coefficient, r radial position, and q the time-dependent adsorption capacity. The exact solution to Eq. (24) for the defined adsorption condition (neglected external film resistance) was given by Crank [76] as follows:

$$\frac{q_t}{q_e} = 1 + \frac{2R}{\pi r}\sum_{n=1}^{\infty}\frac{(-1)^n}{n}\sin\frac{n\pi r}{R}\exp\left[\frac{-D_s t\pi^2 n^2}{R^2}\right] \tag{25}$$

Similarly, the value of D_s from long-time data can be determined by plotting of $\ln(q_t/q_e)$ vs. t. However, the assumption of constant surface concentration for HSDM is likely to be violated at a long time. Therefore, the equation discussed above is generally somewhat valid in a short time.

Similarly, the value of D_s for long-time data can be also determined by plotting of $\ln(1-q_t/q_e)$ vs. t.

$$\ln\left(1-\frac{q_t}{q_e}\right) = \frac{-D_s\pi^2}{R^2}t + \ln\frac{3}{\pi^2} \tag{26}$$

Eq. (26) describes the change rate of surface concentration q_t with time t at any distance R from the center of adsorbent particle during adsorption for a constant boundary condition and developed a non-linear equation for the total mass of adsorbate present on the surface of a unit weight of adsorbent q_t for a specific contact time t. With no film diffusion limitation, this non-linear equation can be generalized into non-dimensional. The HDSM model equations are solved numerically, for a single solute with uniform adsorbent size. However, the assumption of constant surface concentration for HDSM is likely to be violated at a long time. Therefore, the equation discussed above is generally valid in a short time.

The results of diffusional models fitting of kinetic data are given in Table 9.

Analysis of the diffusional process, obtained using the Weber–Morris Eq. (20) (W–M) showed a statistically acceptable correlation as an indication of the low contribution of intra-particular diffusion in the second phase of slow attainment of equilibrium. The results of D–W and HSDM fitting are statistically valid and showed lower dependence on the adsorbent properties. However, the corresponding differences were noted with respect to the analytes. The results obtained show function of the adsorbent textural properties (similar values) where the most prominent factor could be ionic radii and hydration capabilities. The differences in the surface group affinity with respect to specific cation are an additional factor governing variations in the k_{p1} and k_{p2} values of the adsorption process (Table 9).

3.12. Comparison of adsorption performance of $FeAl_2O_3$ and $FeAl_2O_3$APTES with literature data of amino-modified or Al_2O_3-based adsorbents

Comparison of $FeAl_2O_3$ and $FeAl_2O_3$APTES was difficult due to an insufficient number of published literature data, but regardless of this fact it could give valuable information on the adsorption advantageous/deficiency and their possible application. Thus, the comparison of adsorption performance of $FeAl_2O_3$ and $FeAl_2O_3$APTES and other amino-modified adsorbents for Pb^{2+}, Cd^{2+} and Ni^{2+} removal are given in Table 10.

Comparison of q_{max} values shows that aminated PAN nanofibers (q_e 60.6 mg g^{-1}) [77], and two type waste shoe material based on polyurethane, rubber, poly vinyl chloride, ethylene vinyl acetate and ethylene vinyl acetate and formaldehyde (180.20 and 396.31 mg g^{-1}, respectively) [78] both performed at high initial Pb^{2+} and Cd^{2+} concentration. MWCNT-based adsorbents: PEG-MWCNT [41],

Table 9
Rate constants for kinetic modeling of the intraparticular Dunwald–Wagner (D-W), intraparticular homogenous diffusion solid (HDSM), Roginsky–Zeldovich–Elovich (Elovich) and Weber–Morris (W-M, Step 1 and Step 2) models in the adsorption of Pb^{2+}, Cd^{2+} and Ni^{2+} on the $FeAl_2O_3$ and $FeAl_2O_3$APTES adsorbents

Kinetic model	Constants	$FeAl_2O_3$			$FeAl_2O_3$APTES		
		Pb^{2+}	Cd^{2+}	Ni^{2+}	Pb^{2+}	Cd^{2+}	Ni^{2+}
D-W	k_{DW}, min^{-1}	0.00447	0.00407	0.00630	0.00782	0.00351	0.00766
	R^2	0.870	0.924	0.952	0.999	0.925	0.953
HDSM	D_s, $m^2\ s^{-1}$	6.23E-12	5.97E-12	7.97E-12	1.20E-11	5.43E-12	1.19E-11
	R^2	0.806	0.891	0.936	0.984	0.898	0.948
Elovich	a	–6.042	–6.662	–2.842	–6.980	–7.411	–5.408
	b'	3.85622	3.58925	2.70652	4.71592	3.74330	3.59214
	R^2	0.951	0.975	0.979	0.996	0.976	0.960
W-M (Step 1)	k_{p1}, $mg\ g^{-1}\ min^{-0.5}$	2.01825	1.21560	0.87713	2.02802	1.18995	1.32429
	$C_{BL,1}$, $mg\ g^{-1}$	–4.205	–1.958	1.080	–2.214	–1.870	–0.894
	R^2	0.995	0.998	0.997	1.000	0.994	0.987
W-M (Step 2)	k_{p2}, $mg\ g^{-1}\ min^{-0.5}$	0.27348	0.215	0.18318	1.30009	0.21820	0.34687
	$C_{BL,2}$, $mg\ g^{-1}$	9.648	9.107	8.875	2.189	9.312	7.302
	R^2	0.990	0.997	0.998	0.996	0.934	0.991

e-MWCNT [63] and d-MWCNT [36] showed good adsorption capacities, while the nanosize dimension of these adsorbents does not prove consideration of their possible realistic application.

The high surface area of the calcined γ-Al_2O_3 [38], found to be 243 $m^2\ g^{-1}$, contribute to the high adsorption capacity of studied adsorbent (65.67 mg g^{-1}) at high initial Pb^{2+} concentration (200 mg L^{-1}). In a similar study, synthesis of metastable γ-Al_2O_3 by annealing at 650°C–900°C with a particle size in the range 2–4 nm, while temperature increase to higher than 900°C is a favorable condition to obtain α-Al_2O_3 of larger particle size, that is, 80 nm. Obtained results showed that γ-alumina possess significant surface roughness, and higher surface area (136 $m^2\ g^{-1}$) and pore volume (0.06579 $cm^3\ g^{-1}$) in relation to 19.29 $m^2\ g^{-1}$ and 0.00921 $cm^3\ g^{-1}$ found for α-Al_2O_3. Both materials showed low adsorption capacities at a low initial concentration of Pb^{2+} (Table 10) [79]. Improvement of adsorption performances was found for nano-sized γ-Al_2O_3 particles obtained by a modified sol-gel method with 47.08 and 17.22 mg g^{-1} capacities for Pb^{2+} and Cd^{2+} removal, respectively [11]. Production of composite materials based on Al_2O_3 nanoparticles modified with humic acid (Al_2O_3/humic acid), and extract of the walnut shell (Al_2O_3/walnut shell) showed low adsorption capacities: 9.30 and 13.90 mg g^{-1} for Cd^{2+} and 6.80 and 21.00 mg g^{-1} for Ni^{2+} [80]. Similarly to presented results, amino-functionalized silica showed adsorption capacities of 18.25, 12.36 and 57.74 mg g^{-1} with respect to Cd^{2+}, Ni^{2+} and Pb^{2+} cation, respectively [81]. Gathered literature data showed that pure alumina structure showed better adsorption performances with respect to composites obtained therefrom with two open questions: high initial pollutant concentration was used and nanosize dimension make questionable of their applicability in a real water purification processes. Presented comparative analysis, including both $FeAl_2O_3$ and $FeAl_2O_3$APTES adsorbents, indicate their good adsorption performances at applied operational/experimental conditions, with the clear observation that amino modification contributes to the improvement of adsorption performances.

Additionally, adsorption capacities are not only mandatory parameters used for estimation of adsorbent performances. Affinity is a criterion inevitably used for the definition of operational conditions which closely defines the economical aspect of selected adsorption technology. If the design of technology requires moderate to low water quality, the adsorption system should operate near the saturation point with the implication of obtaining high adsorption capacity. Oppositely, the high water purity requires operational condition to relate to the left side of the adsorption isotherm, that is, system operates at low C_i. In this case, adsorption affinity is the most important criterion. Considering the K_L (L mg^{-1}) values from Table 3 with literature data of 0.068 and 0.257 L mg^{-1} for Pb^{2+} and Cd^{2+} [7] showed 32.9–64.4 times higher value for Pb^{2+} and 12.1–17.1 times for Cd^{2+} considering both $FeAl_2O_3$ and $FeAl_2O_3$APTES adsorbents. It indicates that these adsorbents could be used in a process of production moderate to high purity water, that is, above all, it could be applied for the final step of drinking water purification.

4. Conclusions

3DOM alumina was successfully modified with iron oxide and functionalized using APTES to provide the optimal extent of surface modification and adsorption performances. The structural and surface modification of alumina-based adsorbent was confirmed with different characterization methods. Except of beneficial morphological/textural properties of both materials, amino groups introduced on the surface on $FeAl_2O_3$ influences higher adsorption capacity of the $FeAl_2O_3$ APTES. The quality of the isotherm fitting was evaluated from results of statistical analysis, and the

Table 10
Comparison of alumina-based adsorbents with amino-modified adsorbents for Pb^{2+}, Cd^{2+} and Ni^{2+} adsorption

Adsorbent	Ion	C_i, mg L^{-1}	q_e, mg g^{-1}	pH	T, °C	Ref.
Aminated PAN nanofibers	Pb^{2+}	40.0–1,000.0	60.6			[77]
Waste shoe based on polyurethane, rubber, poly vinyl chloride, ethylene vinyl acetate	Cd^{2+}	305.0	180.20	4.9	–	[78]
Waste shoe based on ethylene vinyl acetate and formaldehyde		402.0	396.31	5		
Amino-polyethylene glycol functionalized multiwall carbon nanotube (PEG-MWCNT)	Cd^{2+}	10.0	77.6	8	25	[41]
	Pb^{2+}		47.5	6		
Ethylenediamine-functionalized MWCNT, e-MWCNT	Cd^{2+}	0.1–5.0	25.70	8	45	[63]
Diethylenetriamine functionalized MWCNT, d-MWCNT	Pb^{2+}	5.0–200.0	58.26	6.2	45	[36]
	Cd^{2+}	5.0–100.0	31.45			
γ-Al_2O_3	Pb^{2+}	200.0	65.67	7	25	[47]
γ-Al_2O_3	Pb^{2+}	2.0	0.11	6	25	[79]
α-Al_2O_3			0.16			
γ-Al_2O_3	Pb^{2+}	20.0–150.0	47.08	5	25	[11]
	Cd^{2+}		17.22			
Al_2O_3/walnut shell	Cd^{2+}	50.0	9.30	7	25	[80]
	Ni^{2+}		6.80			
Al_2O_3/humic acid	Cd^{2+}	50.0	13.90	7	25	[80]
	Ni^{2+}		21.00			
Amino-functionalized silica	Cd^{2+}	50.0	18.25	5	25	[81]
	Ni^{2+}		12.36			
	Pb^{2+}		57.74			
$FeAl_2O_3$	Pb^{2+}	10.0	53.35	6	45	This
	Cd^{2+}		29.65			work
	Ni^{2+}		23.40			
$FeAl_2O_3$APTES	Pb^{2+}	10.0	67.46	6	45	This
	Cd^{2+}		49.48			work
	Ni^{2+}		37.77			

best quality of Freundlich isotherm modeling for all cations on $FeAl_2O_3$APTES and Pb^{2+} and Cd^{2+} onto $FeAl_2O_3$ was obtained. Langmuir model better fit of adsorption data for Ni^{2+} onto $FeAl_2O_3$. The second kinetic model best describes Pb^{2+}adsorption on $FeAl_2O_3$, while pseudo-second order fitted well Cd^{2+} and Ni^{2+} onto $FeAl_2O_3$ and Pb^{2+}, Cd^{2+} and Ni^{2+} onto $FeAl_2O_3$APTES. Also, kinetic data fitting for both adsorbents with different diffusional models and Weber–Morris model suggested that the rate-limiting step was diffusion rather than chemical sorption. High adsorption capacities of both adsorbents and good rate of cation uptake indicated on possible applicability of synthesized adsorbents as a modifying agent of the filter of membrane media to be used in a water purification process.

Acknowledgments

This research was financed by the Ministry of Education, Science and Technological Development of the Republic of Serbia as a part of the projects: OI 176018, TR 34011, III 45019 and OI 172057.

Symbols

A' — Arrhenius factor, frequency factor
a — Initial Pb^{2+}, Cd^{2+} and Ni^{2+} adsorption rate, mg g^{-1} min^{-1}
A — Temkin isotherm equilibrium binding constant, L g^{-1}
α — Fractional completion of reactions at time t
B — Dubinin–Radushkevich (D-R) constant, mol^2 kJ^{-2}
b' — Extent of surface coverage and activation energy for chemisorption, g mg^{-1}
b — Temkin isotherm constant
C_{BL} — Constant related to the thickness of the boundary layer
C_e — Equilibrium metal ion concentration in the solution, mg L^{-1}
C_f — Final concentration of ions in the solution, mg L^{-1}
C_i — Initial concentration of ions in the solution, mg L^{-1}
D — Diffusion coefficient of the migrating species
D_s — Intraparticle diffusion coefficient

$\Delta H°$ — Enthalpy change of adsorption, kJ mol^{-1}
$\Delta S°$ — Entropy change of adsorption, J mol^{-1}
$\Delta G°$ — Gibbs free energy, kJ mol^{-1}
E_a — Activation energy, kJ mol^{-1}
ε_p — Particle porosity
h_2 — Initial sorption rate at $t \to 0$, mg g^{-1} min^{-1}
k_{DW} — Dunwald–Wagner isothermal reaction constant
K_F — Freundlich constant
k_i — Intraparticle diffusion rate constant, mg g^{-1} min$^{1/2}$
K_L — Langmuir constant
k_1 — Pseudo-first rate constant, min^{-1}
K — Rate constant of adsorption, min^{-1}
k_2' — Reaction rate constant
k_2 — Second-order rate constant, g mg^{-1} min^{-1}
m — Mass of the adsorbent, g
m_1 — Mass of the pycnometer after being filled with water, g
m_2 — Mass of the pycnometer with wet sample, g
m_3 — Mass of wet sample, g
n^{-1} — Freundlich adsorption intensity parameter
q_e — Adsorbed amount of metal ions at equilibrium, mg g^{-1}
q — Adsorption capacity, mg g^{-1}
q_t — Adsorption capacity at time t, mg g^{-1}
q_m — Maximum adsorption capacity, mg g^{-1}
q_{ref} — Solid phase concentration at time t_{ref}
R_E — Equilibrium factor
r' — Initial radius of the reacting particle
r — Radial position
R_L — Separation factor
R — Universal gas constant, J mol^{-1} K^{-1}
ρ_m — Material density, g mL^{-1}
ρ_{H_2O} — Water density, g mL^{-1}
T — Temperature, K
t — Time, min
V — Volume of solution, L
V_1 — Volume of the pycnometer, 15 mL
V — Volume of the wet sample

References

[1] A.S. Poursani, A. Nilchi, A. Hassani, S. Tabibian, L.A. Amraji, Synthesis of nano–γ–Al_2O_3/chitosan beads (AlCBs) and continuous heavy metals removal from liquid solution, Int. J. Environ. Sci. Technol., 14 (2017) 1459–1468.
[2] L.M. Camacho, S. Ponnusamy, I. Campos, T.A. Davis, S. Deng, In: Evaluation of Novel Modified Activated Alumina as Adsorbent for Arsenic Removal, Handbook of Arsenic Toxicology, Elsevier Inc., 2015, pp. 121–136.
[3] K. Taleb, J. Rusmirović, M. Rancić, J. Nikolić, S. Drmanić, Z. Velicković, A. Marinković, Efficient pollutants removal by amino-modified nanocellulose impregnated with iron oxide, J. Serb. Chem. Soc., 81 (2016) 1199–1213.
[4] M.A. Barakat, New trends in removing heavy metals from industrial wastewater, Arabian J. Chem., 4 (2011) 361–377.
[5] E. Katsou, S. Malamis, K.J. Haralambous, M. Loizidou, Use of ultrafiltration membranes and aluminosilicate minerals for nickel removal from industrial wastewater, J. Membr. Sci., 360 (2010) 234–249.
[6] C.F. Bennani, O. M'hiri, Comparative study of the removal of heavy metals by two nanofiltration membranes, Desal. Wat. Treat., 53 (2015) 1024–1030.
[7] L. Charerntanyarak, Heavy metals removal by chemical coagulation and precipitation, Water Sci. Technol., 39 (1999) 135–138.
[8] Y. Ren, N. Yan, Q. Wen, Z. Fan, T. Wei, M. Zhang, J. Ma, Graphene/δ-MnO_2 composite as adsorbent for the removal of nickel ions from wastewater, Chem. Eng. J., 175 (2011) 1–7.
[9] P. Hadi, J. Barford, G. McKay, Synergistic effect in the simultaneous removal of binary cobalt–nickel heavy metals from effluents by a novel e–waste–derived material, Chem. Eng. J., 228 (2013) 140–146.
[10] W. Liu, W. Sun, Y. Han, M. Ahmad, J. Ni, Adsorption of Cu(II) and Cd(II) on titanate nanomaterials synthesized via hydrothermal method under different NaOH concentrations: role of sodium content, Colloids Surf., A, 452 (2014) 138–147.
[11] S. Tabesh, F. Davar, M. Reza, L. Estarki, Preparation of γ-Al_2O_3 nanoparticles using modified sol-gel method and its use for the adsorption of lead and cadmium ions, J. Alloys Compd., 730 (2018) 441–449.
[12] M. Amrollahi, M.T. Ghaneian, M. Tabatabaee, M.H. Ehrampoush, Highly efficient catalyst for removal of heavy metal ions modified by a novel Schiff base ligand, J. Nanostruct., (2017). Articles in Press, Available Online from 23 April 2017.
[13] A. Chatterjee, J.K. Basu, A.K. Jana, Alumina-silica nano-sorbent from plant fly ash and scrap aluminium foil in removing nickel through adsorption, Powder Technol., 354 (2019) 792–803.
[14] A. Teimouri, N. Ghased, S.G. Nasab, S. Habibollahi, Statistical design of experiment as a tool for optimization of methylene blue sorption on CS/MCM-41/nano-γ alumina as a novel and environmentally friendly adsorbent: isotherm and kinetic studies, Desal. Wat. Treat., 139 (2019) 327–341.
[15] M.T. Sultan, H.S. Al-Lami, A.H. Al-Dujiali, Synthesis and characterization of alumina-grafted acrylic acid monomer and polymer and its adsorption of phenol and p-chlorophenol, Desal. Wat. Treat., 150 (2019) 192–203.
[16] J. Čejka, Organized mesoporous alumina: synthesis, structure and potential in catalysis, Appl. Catal., A, 254 (2003) 327–338.
[17] A. Stein, R.C. Schroden, Colloidal crystal templating of three–dimensionally ordered macroporous solids: materials for photonics and beyond, Curr. Opin. Solid State Mater. Sci., 5 (2001) 553–564.
[18] L.Z. Fan, Y.S. Hu, J. Maier, P. Adelhelm, B. Smarsly, M. Antonietti, High electroactivity of polyaniline in supercapacitors by using a hierarchically porous carbon monolith as a support, Adv. Funct. Mater., 17 (2007) 3083–3087.
[19] M. Farahmandjou, N. Golabiyan, Synthesis and characterization of alumina (Al_2O_3) nanoparticles prepared by simple sol-gel method, Int. J. Bio-Inorg. Hybr. Nanomater., 5 (2016) 73–77.
[20] R.J. Kalbasi, M. Kolahdoozan, M. Rezaei, Synthesis and characterization of polyvinyl amine-SiO_2-Al_2O_3 as a new and inexpensive organic-inorganic hybrid basic catalyst, J. Ind. Eng. Chem., 18 (2012) 909–918.
[21] Y. Xin, Y. Takeuchi, M. Hattori, T. Shirai, Enhanced electrical conductivity of alumina/nano-carbon ceramic composite via iodine impregnation of gel-casted alumina body and reductive sintering, J. Eur. Ceram. Soc., 39 (2019) 4440–4444.
[22] A. Majedi, A. Abbasi, F. Davar, Green synthesis of zirconia nanoparticles using the modified Pechini method and characterization of its optical and electrical properties, J. Sol–Gel Sci. Technol., 77 (2016) 542–552.
[23] T.C. Gomes, D. Kumar, L. Fugikawa-Santos, N. Alves, J. Kettle, Optimization of the anodization processing for aluminum oxide gate dielectrics in ZnO thin film transistors by multivariate analysis, ACS Comb. Sci., 21 (2019) 370–379.
[24] Z. Zang, A. Nakamura, J. Temmyo, Single cuprous oxide films synthesized by radical oxidation at low temperature for PV application, Opt. Express, 21 (2013) 11448–11456.
[25] M.H. Yousefi, M.M. Zerafat, M.S. Doodeji, S. Sabbaghi, Investigation of dip-coating parameters effect on the performance of alumina-polydimethylsiloxane nanofiltration membranes for desalination, J. Water Environ. Nanotechnol., 2 (2017) 235–242.
[26] Z. Zang, X. Zeng, J. Du, M. Wang, X. Tang, Femtosecond laser direct writing of microholes on roughened ZnO for output power enhancement of InGaN lightemitting diodes, Opt. Lett., 41 (2016) 3463–3466.

[27] S.A.C. Carabineiro, P.B. Tavares, J.L. Figueiredo, Gold on oxide-doped alumina supports as catalysts for CO oxidation, Appl. Nanosci., 2 (2012) 35–46.
[28] E. Soleimani, N. Zamani, Surface modification of alumina nanoparticles: a dispersion study in organic media, Acta Chim. Slov., 64 (2017) 644–653.
[29] L.A.S.A. Prado, M. Sriyai, M. Ghislandi, A.B. Timmonsb, K. Schulte, Surface modifcation of alumina nanoparticles with silane coupling agents, J. Braz. Chem. Soc., 21 (2010).
[30] N.K. Koju, X. Song, Q. Wang, Z. Hu, C. Colombo, Cadmium removal from simulated groundwater using alumina nanoparticles: behaviors and mechanisms, Environ. Pollut., 240 (2018) 255–266.
[31] S.E. Cabaniss, Forward modeling of metal complexation by NOM: II. Prediction of binding site properties, Environ. Sci. Technol., 45 (2011) 3202–3209.
[32] N.M. Bravaya, S.L. Saratovskikh, A.N. Panin, E.E. Faingol'd, I.V. Zharkov, O.N. Babkina, S.G. Vasil'ev, M.L. Bubnova, V.I. Volkov, M.V. Lobanov, Influence of silane coupling agent on the synthesis and properties of nanocomposites obtained via in situ catalytic copolymerization of ethylene and propylene in the presence of modified Nafen™ Al_2O_3 nanofibers, Polymer, 174 (2019) 114–122.
[33] A. Drah, N.Z. Tomić, Z. Veličić, A.D. Marinković, Ž. Radovanović, Z. Veličković, R. Jančić-Heinemann, Highly ordered macroporous γ–alumina prepared by a modified sol–gel method with a PMMA microsphere template for enhanced Pb^{2+}, Ni^{2+} and Cd^{2+} removal, Ceram. Int., 43 (2017) 13817–13827.
[34] L.S. Eaton, A.D. Clesceri, Standard Methods for the Examination of Water and Wastewater, 22nd ed., American Water Works Association (AWWA), Washington, D.C., 2012.
[35] Z.S. Veličković, G.D. Vuković, A.D. Marinković, M.S. Moldovan, A.A. Perić-Grujić, P.S. Uskoković, M.D. Ristić, Adsorption of arsenate on iron(III) oxide coated ethylenediamine functionalized multiwall carbon nanotubes, Chem. Eng. J., 181–182 (2012) 174–181.
[36] G.D. Vuković, A.D. Marinković, S.D. Škapin, M.Đ. Ristić, R. Aleksić, A.A. Perić–Grujić, P.S. Uskoković, Removal of lead from water by amino modified multi–walled carbon nanotubes, Chem. Eng. J,, 173 (2011) 855–865.
[37] Y.K. Park, E.H. Tadd, M. Zubris, R. Tannenbaum, Size-controlled synthesis of alumina nanoparticles from aluminum alkoxides, Mater. Res. Bull., 40 (2005) 1506–1512.
[38] L. Wu, Z. Yin, Sulfonic acid functionalized nano γ–Al_2O_3 catalyzed per–Oacetylated of carbohydrates, Carbohydr. Res., 365 (2013) 14–19.
[39] Y. Wang, W. Eli, L. Zhang, H. Gao, Y. Liu, P. Li, A new method for surface modification of nano–$CaCO_3$ and nano–Al_2O_3 at room temperature, Adv. Powder Technol., 21 (2010) 203–205.
[40] T.F. Gan, B.Q. Shentu, Z.X. Weng, Modification of CeO_2 and its effect on the heat–resistance of silicone rubber, Chin. J. Polym. Sci., 26 (2008) 489–494.
[41] Z. Veličković, Z. Bajić, M. Ristić, V. Đokić, A. Marinković, P. Uskoković, M. Vuruna, Modification of multi–wall carbon nanotubes for the removal of cadmium, lead and arsenic from wastewater, Dig. J. Nanomater. Biostruct., 8 (2013) 501–511.
[42] H. Sontheimer, J.C. Crittenden, R.S. Scott, Activated Carbon for Water Treatment. In Activated carbon for water treatment; DVGW-Forschungsstelle, Engler-Bunte-Institut, Universitat Karlsruhe, 1988, pp. 66–67.
[43] G. Lazouzi, M.M. Vuksanović, N.Z. Tomić, M. Mitrić, M. Petrović, V. Radojević, R. Jančić-Hainemann, Optimized preparation of alumina based fillers for tuning composite properties, Ceram. Int., 44 (2018) 7442–7449.
[44] D. Han, X. Li, L. Zhang, Y. Wang, Z. Yan, S. Liu, Hierarchically ordered meso/ macroporous γ–alumina for enhanced hydrodesulfurization performance, Microporous Mesoporous Mater., 158 (2012) 1–6.
[45] B. Arkles, Silane Coupling Agents: Connecting Across Boundaries, Gelest, Inc., Morrisville, PA, 3rd ed., 2014.
[46] G. Arslan, M. Özmen, B. Gündüz, X.G. Zhan, M. Ersöz, Surface modification of glass beads with an aminosilane monolayer, Turk. J. Chem., 30 (2006) 203–210.
[47] A. Bhat, G.B. Megeri, C. Thomas, H. Bhargava, C. Jeevitha, S. Chandrashekar, G.M. Madhu, Adsorption and optimization studies of lead from aqueous solution using γ–alumina, J. Environ. Chem. Eng., 3 (2015) 30–39.
[48] S. Agarwal, I. Tyagi, V.K. Gupta, M.H. Dehghani, J. Jaafari, D. Balarak, M. Asif, Rapid removal of noxious nickel(II) using novel γ–alumina nanoparticles and multiwalled carbon nanotubes: kinetic and isotherm studies, J. Mol. Liq., 224 (2016) 618–623.
[49] N. Obradović, S. Filipović, S. Marković, M. Mitrić, J. Rusmirović, A. Marinković, V. Antić, V. Pavlović, Influence of different pore–forming agents on wollastonite microstructures and adsorption capacities, Ceram. Int., 43 (2017) 7461–7468.
[50] M.A. Mahmoud, Kinetics and thermodynamics of aluminum oxide nanopowder as adsorbent for Fe(III) from aqueous solution, Beni–Suef Univ. J. Appl. Sci., 4 (2015) 142–149.
[51] M. Bozorgi, S. Abbasizadeh, F. Samani, S.E. Mousavi, Performance of synthesized cast and electrospun PVA/chitosan/ZnO-NH_2 nano-adsorbents in single and simultaneous adsorption of cadmium and nickel ions from wastewater, Environ. Sci. Pollut. Res., 25 (2018) 17457–17472.
[52] M.M. Tehrania, S. Abbasizadehb, A. Alamdaric, S.E. Mousavi, Prediction of simultaneous sorption of copper(II), cobalt(II) and zinc(II) contaminants from water systems by a novel multi-functionalized zirconia nanofiber, Desal. Wat. Treat., 62 (2017) 403–417.
[53] M. Karanac, M. Đolić, Đ. Veljović, V. Rajaković-Ognjanović, Z. Veličković, V. Pavićević, A. Marinković, The removal of Zn^{2+}, Pb^{2+}, and As(V) ions by lime activated fly ash and valorization of the exhausted adsorbent, Waste Manage., 78 (2018) 366–378.
[54] Y. Zhai, W. Zhou, W. Wei, J. Qu, J. Lei, Z. Su, G. Ma, Functional gigaporous polystyrene microspheres facilitating separation of poly(ethylene glycol)–protein conjugate, Anal. Chim. Acta, 712 (2012) 152–161.
[55] J.D. Rusmirović, N. Obradović, J. Perendija, A. Umićević, A. Kapidžić, B. Vlahović, V. Pavlović, A.D. Marinković, V.B. Pavlović, Controllable synthesis of Fe_3O_4-wollastonite adsorbents for efficient heavy metal ions/oxyanions removal, Environ. Sci. Pollut. Res. Int., 26 (2019) 12379–12398.
[56] D. Budimirović, Z.S. Veličković, V.R. Djokić, M. Milosavljević, J. Markovski, S. Lević, A.D. Marinković, Efficient As(V) removal by α–FeOOH and α–FeOOH/α–MnO_2 embedded PEG–6–arm functionalized multiwall carbon nanotubes, Chem. Eng. Res. Des., 119 (2017) 75–86.
[57] S. Abbasizadeh, A.R. Keshtkar, M.A. Mousavian, Sorption of heavy metal ions from aqueous solution by a novel cast PVA/TiO_2 nanohybrid adsorbent functionalized with amine groups, J. Ind. Eng. Chem., 20 (2014) 1656–1664.
[58] V. Hernández-Morales, R. Nava, Y.J. Acosta-Silva, S.A. Macías-Sánchez, J.J. Pérez-Bueno, B. Pawelec, Adsorption of lead(II) on SBA–15 mesoporous molecular sieve functionalized with–NH_2 groups, Microporous Mesoporous Mater., 160 (2012) 133–142.
[59] W. Stumm, Aquatic Surface Chemistry: Chemical Processes at the Particle-Water Interface, John Wiley & Sons, 1987, p. 87.
[60] H. Hohl, W. Stumm, Interaction of Pb^{2+} with hydrous γ-Al_2O_3, J. Colloid Interface Sci., 55 (1976) 281–288.
[61] O. Takahashi, K. Saito, S. Yamamoto, N. Nishimura, Cadmium removal from simulated–ethylenediamine and–ammonia exciplexes. Comparison with experiments, Chem. Phys. Lett., 207 (1993) 379–383.
[62] G. Ma, A. Fischer, R. Nieuwendaal, K. Ramaswamy, S.E. Hayes, Cd(II)–ethylenediamine mono–and bimetallic complexes–Synthesis and characterization by ^{113}Cd NMR spectroscopy and single crystal X-ray diffraction, Inorg. Chim. Acta, 358 (2005) 3165–3173.
[63] G.D. Vuković, A.D. Marinković, M. Čolić, M.Đ. Ristić, R. Aleksić, A.A. Perić-Grujić, P.S. Uskoković, Removal of cadmium from aqueous solutions by oxidized and ethylenediamine–functionalized multi–walled carbon nanotubes, Chem. Eng. J., 157 (2010) 238–248.
[64] S. Lagergren, About the theory of so-called adsorption of soluble substances, K. Sven. Vetenskapsakad., 24 (1898) 1–39.

[65] Z. Ren, G. Zhang, J. Paul Chen, Adsorptive removal of arsenic from water by an iron-zirconium binary oxide adsorbent, J. Colloid Interface Sci., 358 (2011) 230–237.
[66] S. Lazarević, V. Marjanović, I. Janković-Častvan, L. Živković, Dj. Janaćkovića, R. Petrović, Effective removal of Reactive Orange 16 dye from aqueous solution by aminefunctionalized sepiolites, Desal. Wat. Treat., 163 (2019) 376–384.
[67] D. Mohan, V.K. Gupta, S.K. Srivastava, S. Chander, Kinetics of mercury adsorption from wastewater using activated carbon derived from fertilizer waste, Colloid Surf., A, 177 (2001) 169–181.
[68] S. Glasston, K.J. Laidler, H. Eyring, The Theory of Rate Processes, McGraw-Hill, New York, 1941.
[69] M.J.D. Low, Kinetics of chemisorption of gases on solids, Chem. Rev., 60 (1960) 267–312.
[70] F.C. Wu, R.L.Tseng, R.S. Juang, Characteristics of Elovich equation used for the analysis of adsorption kinetics in dye-chitosan systems, Chem. Eng. J., 150 (2009) 366–373.
[71] W.J. Weber, J.C. Moris, Kinetics of adsorption on carbon from solution, J. Sanit. Eng. Div., 89 (1963) 31–59.
[72] H. Dünwald, C. Wagner, Methodik der Messung von Diffusiongeschwindigkeiten bei Losungsvorgangen von Gasen in festen Phasen (Measurement of Diffusion Rate in the Process of Dissolving Gases in Solid Phases), Zeitschrift für Phys. Chemie B24, pp. 53–58, 1934.
[73] Q.I.U. Hui, L.V. Lu, B.C. Pan, Q.J. Zhang, W.M. Zhang, Q.X. Zhang, Critical review in adsorption kinetic models, Univ. Sci. A, 10 (2009) 716–724.
[74] B. Serin, R.T. Ellickson, Determination of diffusion coefficients, J. Chem. Phys., 9 (1941) 742.
[75] D.O. Cooney, Adsorption Design for Wastewater Treatment, Lewis Publishers, Boca Raton, 1999.
[76] J. Crank, Mathematics of Diffusion, Oxford at the Clarendon Press, London, UK, 1956.
[77] P. Kampalanonwat, P.Supaphol, Preparation and adsorption behavior of aminated electrospun polyacrylonitrile nanofiber mats for heavy metal ion removal, ACS Appl. Mater. Interfaces, 2 (2010) 3619–3627.
[78] M. Iqbal, N. Iqbal, I.A. Bhatti, N. Ahmad, M. Zahid, Response surface methodology application in optimization of cadmium adsorption by shoe waste: a good option of waste mitigation by waste, Ecol. Eng., 88 (2016) 265–275.
[79] M.A. Ahmed, S.T. Bishay, R. Ramadan, Water detoxification using gamma and alfa alumina nanoparticles prepared by micro emulsion route, Nano. Technol. Nano. Sci. Ind. J., 9 (2015) 064–074.
[80] S. Mahdavi, M. Jalali, A. Afkhami, Heavy metals removal from aqueous solutions by Al_2O_3 nanoparticles modified with natural and chemical modifiers, Clean. Technol. Environ. Policy, 17 (2015) 85–102.
[81] A. Heidari, H. Younesi, Z. Mehrabanb, Removal of Ni(II), Cd(II), and Pb(II) from a ternary aqueous solution by amino functionalized mesoporous and nano mesoporous silica, Chem. Eng. J., 153 (2009) 70–79.